Applied Surface Science 615 (2023) 156212

Contents lists available at ScienceDirect

Applied Surface Science

journal homepage: www.elsevier.com/locate/apsusc

Full length article

Embossing of silicon with an ultrashort laser pulse diffracted by a bubble in liquid

S.A. Romashevskiy [a,*], A.I. Ignatov [b,c], V.V. Zhakhovsky [a,b], E.M. Eganova [e], E.A. Pershina [e], N.A. Inogamov [d,a], S.I. Ashitkov [a]

[a] Joint Institute for High Temperatures, RAS, 13/2 Izhorskaya st., 125412 Moscow, Russian Federation
[b] Dukhov Automatics Research Institute (VNIIA), 22 Sushchevskaya st., 127030 Moscow, Russian Federation
[c] National Research Moscow State University of Civil Engineering, 26 Yaroslavskoye sh., 129337 Moscow, Russian Federation
[d] Landau Institute for Theoretical Physics, RAS, 1A Semenova av., 142432 Chernogolovka, Russian Federation
[e] Institute of Nanotechnology of Microelectronics, RAS, 32A Leninsky Pr., 119991 Moscow, Russian Federation

ARTICLE INFO

Keywords:
Silicon
Bubble
Ultrashort laser pulses
Diffraction
Liquid
Melting

ABSTRACT

Laser-assisted nanostructuring of silicon interfaces provides a unique procedure for leading-edge technologies. We report on a new embossing technique with tightly focused Gaussian-shaped ultrashort laser pulses near the ablation threshold in liquid. We take advantage of a primary microbubble for controllable spatial-modulation of light intensity of succeeding pulses. Such a bubble, generated in liquid near the molten silicon surface by the first pulse, serves as an obstacle for the second pulse following with a sub-millisecond time delay, to produce a diffraction ring pattern. Variation of laser intensity can be utilized to guide the diffraction patterns. Thus the various annular patterns deeply embossed up to hundreds nanometers on the surface are produced with high reproducibility. Morphology of modified surface layer is investigated in detail using atomic-force microscopy, as well as scanning and transmission electron microscopies. Full-wave EM modeling of laser beam diffraction by the bubbles with various radii and shapes shows that the peak intensity in silicon is up to 1.7 times higher than in bubble-free liquid. Atomistic simulation of ultrafast heating with such a diffraction peak reveals that an annular microdimple surrounded by rims is formed by high-gradient pressure in molten silicon to be frozen after several nanoseconds.

1. Introduction

In the last decade, selective high-precision modification of nanolayers of diverse materials and creation of various kinds of micro/nanostructures with ultrafast lasers acquired great significance for solar power and electronics industries, as well as planar photonics with metasurfaces and surface-enhanced Raman spectroscopy (SERS) applications [1–9]. In general, the state-of-the-art technology of materials processing with ultrashort laser pulses combining with laser scanning systems and beam multiplexing methods allows modifying a particular layer of material with a required pattern at unprecedented high speed without needing in photolithographic masking and high-cost clean rooms [10,11].

To meet the specific requirements of materials processing, the ambient environment and typical laser parameters such as fluence, spot size, wavelength, number of pulses and polarization, are usually controlled. Recently, temporal and spatial modulation of ultrashort laser pulses has been actively exploited to achieve high efficiency in fabricating micro- and nanostructures, as well as to create certain types of modifications on the surface and inside materials [12]. For example, sharp-pointed microneedles and nanoprotrusions were formed on silicon in air with laser pulses having a doughnut-shaped intensity profile due to the radial inward motion of molten silicon [13–15]. In addition, when using an optical vortex beam with orbital angular momentum, it is possible to obtain chiral microprotrusions [16–18]. It was demonstrated that all these needle-like structures can be potentially used for surface-enhanced infrared absorption [19] and multi-wavelength biosensing [20].

In recent years, much attention has also been addressed to pulsed laser ablation in liquid (PLAL). Here, apart from efficient mass production of nanoparticles [21], ultrashort laser pulses when tightly focused onto a solid material surface under liquid confinement enable the control over the surface morphology at the nanoscale and even below, allowing to produce subnanoscale protrudings and subnanostructured interfaces [22]. Moreover, the structures formed in liquid are generally

* Corresponding author.
E-mail addresses: sa.romashevskiy@gmail.com (S.A. Romashevskiy), ashitkov11@yandex.ru (S.I. Ashitkov).

https://doi.org/10.1016/j.apsusc.2022.156212
Received 4 November 2022; Received in revised form 5 December 2022; Accepted 21 December 2022
Available online 23 December 2022

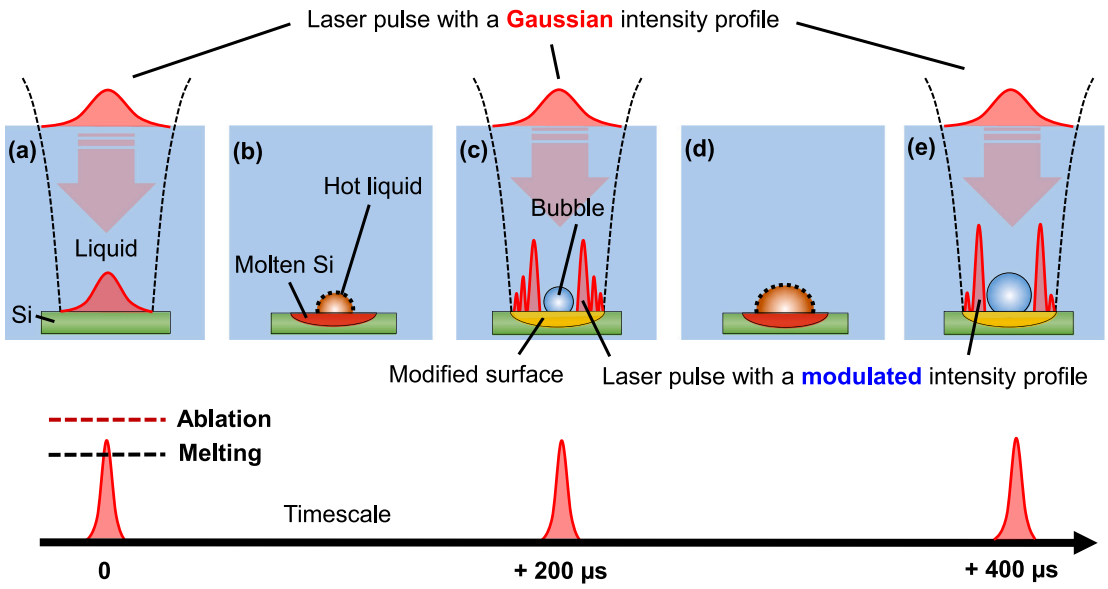

Fig. 1. Chart explaining the process of spatial modulation of laser radiation due to the diffraction of the second and third pulses by a bubble formed as a result of heating the silicon surface in liquid by the previous pulse. The material surface under liquid confinement is irradiated with several laser pulses delayed by 200 μs and having a Gaussian intensity profile, the incident laser fluence is slightly higher than the melting threshold. (a) The irradiation with the first Gaussian-shaped pulse results in melting the silicon surface and overheating of a thin liquid layer which later on results in the generation of a bubble (b). (c) The irradiation with the second Gaussian-shaped pulse results in laser radiation diffraction by the bubble and exposing the surface to irradiation by a spatially modulated intensity profile in the form of a diffraction ring pattern. This, in turn, leads to the generation of a bigger bubble (d) which also serves as a modulator for the third pulse and thus contributes to the appearance of another diffraction ring pattern (e).

smoother and cleaner compared to those produced in gas or vacuum environments [22,23]. However, in contrast to laser irradiation of materials in gas or vacuum, even single-pulse irradiation at below-ablation threshold fluences in liquid besides heating the sample itself results in inevitable overheating of a thin near-surface layer of liquid, which later on leads to the formation of vapor and gas bubbles near the irradiated surface of a material [24]. In particular, it was demonstrated that the bubble lifetime in ultrafast laser-induced liquid breakdown and PLAL experiments depends on the bubble size (which is determined by the absorbed laser energy) and its gas composition, and the liquid viscosity. The bubble lifetime can span from hundreds microseconds in water [25–28] to several seconds in viscous liquids [29].

The phenomenon of laser-assisted bubble generation near the irradiated surface is well known in PLAL field and has been actively used to generate chemically pure nanoparticles [21,30]. On the one hand, the hot liquid layer which is diffusely mixed with the target substance is a kind of “reactor” in which nanoparticles are formed [30,31]. But in most PLAL applications, such as surface treatment, generation of nanoparticles and laser shock peening, laser fluences are significantly higher the ablation threshold of the material, which leads to the formation of deep craters (tens to hundreds of nanometers) and large long-lived bubbles with diameters that can significantly exceed the laser focal spot [21]. On the other hand, the generated bubble is a negative factor since it shields the surface of the material from the interaction with the subsequent pulses following at a repetition rate from several kHz to tens of MHz [10]. On the contrary, in Refs. [24,32] we have shown that such an adverse effect can be useful in producing specific annular embossed patterns (so-called circular ripple patterns [24]) on the silicon surface in viscous liquid with two tightly focused Gaussian-shaped femtosecond laser pulses separated by a sub-millisecond delay. The bubble, generated in liquid near the molten surface by the first pulse, serves as a microscale dynamic obstacle for spatial modulation of the intensity profile of the second pulse. This process is schematically illustrated in Fig. 1.

The spatially modulated intensity distribution of the second pulse is projected onto the surface of the material in the form of a diffraction ring pattern (circular fringe pattern). As a result, annular embossed patterns are formed on the surface of the material, which similar to diffraction rings consist of alternating annular maxima and minima of the surface relief — annular microdimples (grooves) and protruding rims with a height and depth from several to hundreds of nanometers.

The specific type of diffraction ring pattern and, consequently, the annular embossed pattern formed on the surface, is determined only by the energy of the laser pulses (at constant delay). The first pulse with a Gaussian intensity distribution is a “seed” pulse since a bubble is formed later on (surface modification could be negligible, especially at fluences near the melting threshold). The second pulse initially with a Gaussian intensity distribution as a result of diffraction by the bubble spatially reshapes into a modulated intensity distribution in the form of diffraction rings. The energy of the second pulse now determines the level of radiation intensity in the diffraction pattern. It is important that at a constant delay between the first and second pulses, it is the energy deposited in the material by the first pulse that will subsequently determine the type of diffraction pattern of the second pulse. It occurs since the degree of superheating of the liquid layer and, accordingly, the diameter of the generated bubble depends on the energy deposited into the material, i.e. the more energy is deposited into the material, the bigger bubble forms.

However, this effect takes place in a limited range of fluences and time delays between pulses, the latter is determined by the bubble lifetime in the liquid. If the time delay between two pulses exceeds the bubble lifetime (which implies irradiation with two Gaussian-shaped pulses), then another type of surface structures is formed — the well-known laser-induced periodic surface structures (LIPSS) oriented perpendicular to the laser polarization [24]. The fluence range has a lower limit which is the silicon melting threshold (near half the ablation threshold) and an upper limit when the bubble diameter becomes comparable with the laser focal spot and starts shielding the incident laser radiation (nearly two times the ablation threshold). These limits make it difficult to observe this effect as PLAL experiments on mass production of nanoparticles are usually carried out at rather high fluences [10,21]. According to our data, this effect has not been observed before by other research groups.

Since the bubble formation time in liquids is incomparably longer than the ultrashort laser pulse duration (which is 100–300 fs) [25,33], the laser pulse diffraction by a bubble is excluded in experiments

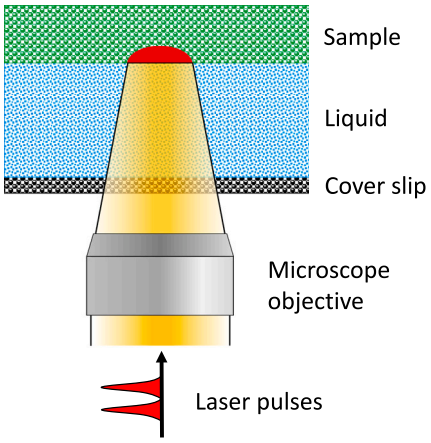

Fig. 2. Layout of liquid layer and silicon sample irradiated by laser pulses in experiments. Gravity is directed from the sample to liquid, which is supported by a glass slip. Two delayed laser pulses are focused onto the liquid/silicon interface.

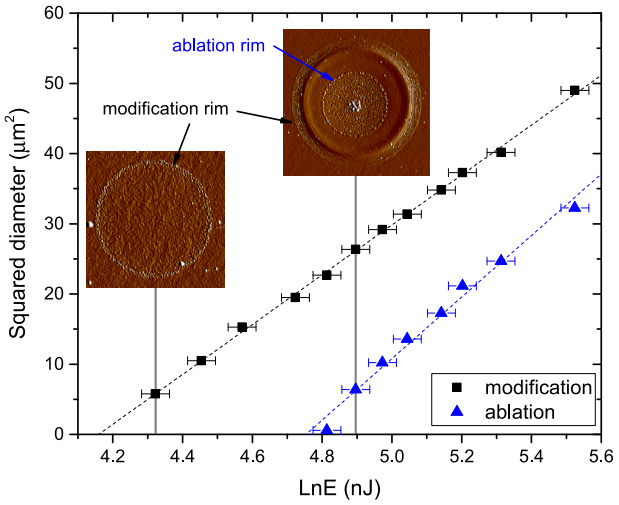

Fig. 3. Squared diameter of each rim related to surface modification (black squares) and ablation (blue triangles) versus logarithm of the energy of incident laser pulses at a wavelength of 1028 nm. The AFM scans are shown in insets with vertical lines indicating the corresponding energy of laser pulses.

with single laser pulses. However, according to the published data, several research groups have previously observed similar circular ripple patterns (with a spatial period comparable to a laser wavelength) formed on the surface of silicon immersed into a liquid (water) as a result of exposure to a single femtosecond laser pulse in a wide fluence range from $F = [0.015–3]$ J/cm^2 at (100–200 fs, 400 nm) to $F = 12$ J/cm^2 at (130 fs, 800 nm) [34–39]. It is worth noting that the observed circular ripple patterns significantly varied in size and number from experiment to experiment, and their position on the surface had a random nature. However, despite their visual similarity with the circular ripple patterns produced on metal-coated silicon after illuminating in air with a diffraction ring pattern (or circular fringe pattern) formed as a result of scattering of a Gaussian-shaped nanosecond laser pulse on pre-existing suspended dust particles in front of the target [40], the authors of the above-mentioned studies had not considered the possibility of diffraction of a laser pulse by pre-existing suspended particles or bubbles in liquid [41]. On the contrary, no circular ripple patterns (with a spatial period comparable to a laser wavelength) were found after exposure to a single femtosecond laser pulse in many other studies (including this paper) at different laser wavelengths and in a wide range of fluences, as well as in various liquids (water, oil) [22,42–48].

This paper presents both experimental results and theoretical explanation of the process of formation of various types of annular embossed patterns on the silicon surface in liquid after the irradiation with two pulses separated by a sub-millisecond delay. The experimental data obtained in media with different viscosities (glycerol, water) in a wide range of fluences, as well as at different wavelengths and number of laser pulses are presented. The surface morphology and superficial layer structure of annular embossed patterns were investigated in detail using atomic-force microscopy (AFM), scanning electron microscopy (SEM) and transmission electron microscopy (TEM). The diffraction of light by a bubble and the mechanism of melt flow in liquid environment were also studied numerically with electromagnetic and atomistic simulations, respectively. The possibilities of the control over the specific pattern through the laser intensity variation, laser wavelength and a number of pulses are shown.

2. Experimental setup

An ytterbium fiber laser that provides Gaussian-shaped linearly-polarized 270-fs laser pulses at a central wavelength of 1028 nm and at the maximum repetition rate of 5 kHz was used in the experiments. The laser beam was focused at a normal incidence onto a sample's surface to a spot of ~ 6 μm diameter at 1/e level with a microscope objective UPlanFL N Olympus 20X/0.5. The sample was an n-type commercially-available polished silicon wafer with crystal orientation (111), conductivity of 3–7 kΩ cm, arithmetic average roughness of 0.1 nm (R_a), and thickness of 460 μm. The sample was placed in a Petri dish [24] filled with a glycerol $C_3H_8O_3$ (density of 1.260 g/cc and dynamic viscosity of 1480 mPa s) or distilled water (density of 0.998 g/cc and dynamic viscosity of 1 mPa s) both at 20 °C. Such liquids were chosen as the liquid composition and viscosity significantly affect the dynamics and lifetime of laser-induced bubbles. The thicknesses of the entrance glass (cover slip) of the Petri dish and liquid layer are 0.15 and 0.9 mm, respectively.

The experiments were carried out at the fundamental laser wavelength (1028 nm) and its second harmonic (514 nm). For experiments with the frequency-doubled wavelength (514 nm) a standard set of LBO crystal and IR blocking filter was used. A schematic diagram of the experimental setup is shown in Fig. 2. Note that the laser radiation is upward incident on the sample (against the gravitational force).

The silicon surface was irradiated with single laser pulses, as well as with two and three laser pulses of the same energy and delayed by 200 μs (5 kHz) over the fluence range near the ablation threshold — from $F_0 = 0.62F_a$ to $1.68F_a$. Here F_0 is the incident laser fluence at the center of the spot, F_a — the ablation threshold. The values of F_a (along with the modification threshold F_{mod}) and laser spot diameter were measured in glycerol in a single shot mode using a method proposed by Liu [49] (Fig. 3). Linear approximation of the experimental data indicates the absence of optical breakdown and other nonlinear phenomena in the liquid in the above-mentioned fluence range. The outer rim of modified surface, resolved by atomic-force microscopy, practically corresponds to the boundary of the melting region in silicon, truly resolved only by optical microscopy [50]. The modification threshold F_{mod} was estimated by measuring the outer rim which was considered as the boundary of the modification of the silicon as the surface topography outside this region indicated of no other modifications. One should also keep in mind that the modification threshold F_{mod} is slightly higher the melting threshold F_{melt} as it is located inside the melting region [50]. The crown-like rim surrounding the central zone with a significantly higher surface roughness was considered as the boundary of ablation [22]. The measured values of F_a and F_{mod} shown in Table 1 are in good agreement with literature data [50]. Note that all the mentioned here fluences are estimated for

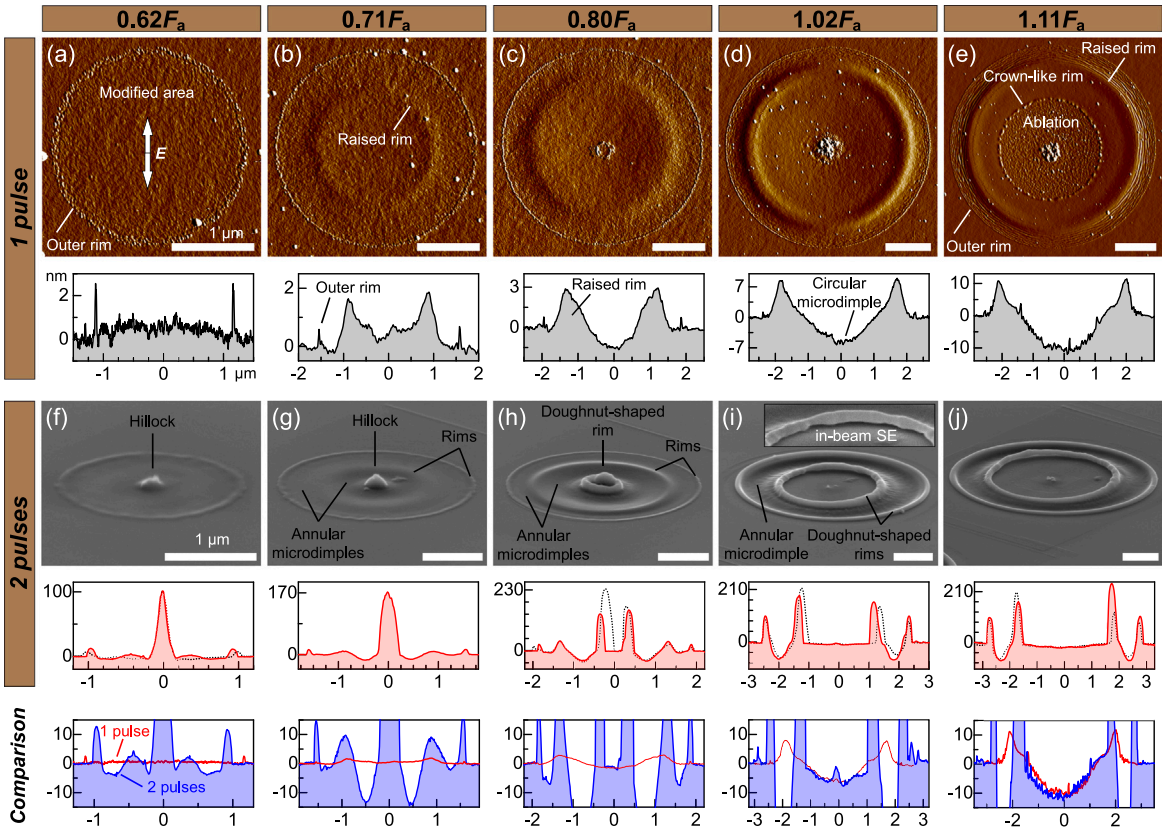

Fig. 4. The surface modifications induced with single (a–e) and two (f–j) laser pulses delayed by 200 μs at a wavelength of 1028 nm in glycerol. The AFM scans (amplitude error), corresponding X and Y cross-sections, and SEM images are shown. The white double-headed arrow indicates the direction of the laser polarization. X- and Y-axes on all the cross-sections are in μm and nm, respectively.

Table 1
Modification and ablation thresholds of silicon, and laser spot diameters for two wavelengths in glycerol and distilled water. Notice that incident fluences are shown.

	Glycerol		Water
Irradiation wavelength (nm)	1028	514	514
Ablation threshold F_a (J/cm^2)	0.44	0.29	0.31
Modification F_{mod} (J/cm^2)	0.23	0.16	0.17
Spot diameter D at 1/e (μm)	5.9	5.8	6.6

a Gaussian-shaped pulse normally emitted by the laser. The energy of the incident laser pulses was measured with 2% uncertainty.

The laser-induced silicon surface modifications were investigated by means of atomic-force microscopy (AFM, Veeco MultiMode V) in tapping mode (tip radius < 10 nm, resolution at z-direction is 0.05 nm), scanning electron microscopy (SEM, Tescan MIRA 3) using secondary electrons detectors (SE and in-beam SE) and transmission electron microscopy (TEM, JEOL JEM 2100 Plus). For TEM studies of the modified crystalline structure of the surface layer the lamellae with a thickness of about 100 nm were prepared using the focused ion beam (FIB) method. To protect the samples from the effects of FIB during cutting, a 200–250 nm thick layer of platinum was deposited onto the surface. TEM studies were carried out at an accelerating voltage of 200 kV.

After the laser processing the silicon samples were only rinsed in distilled water omitting ultrasonic cleaning procedure in order not to induce any damage to surface structures as was previously realized in Ref. [24].

3. Experimental results and discussion

The structures induced on the silicon surface in glycerol with single and two pulses (delayed by 200 μs) over the near-ablation fluence range $F_0 = [0.62–1.11]F_a$ at a wavelength of 1028 nm are shown in Fig. 4. The upper panel shows a variety of surface structures formed after irradiation with a single pulse with increasing fluence. The middle panel shows the structures formed after irradiation with two pulses at the same fluences. And, finally, comparison in surface topography between these two regimes is shown in the lower panel. As shown in Fig. 4, the control over the specific surface pattern upon irradiation with two pulses delayed by 200 μs could be easily realized only through the laser intensity variation, which allows producing a wide range of structures.

3.1. Irradiation with single pulses

The irradiation of the silicon surface with a single Gaussian-shaped laser pulse over the near-ablation fluence range in liquids normally results in bowl-shaped microdimples (or microcavities) surrounded by several protruding ring-shaped structures of various morphology, i.e. outer, raised and crown-like rims as in Fig. 4(c–e) [22].

However, at lower fluences, namely just above the melting threshold $F_0 = 0.62F_a$, the irradiated area is mainly featured by a thin outer rim surrounding the central area that holds very slight changes in superficial topography [Fig. 4(a)]. In addition to this subtle modification, other characteristic structures are formed with increasing fluence. To begin with, there forms a raised rim associated with radial hydrodynamic motion of the melt [Fig. 4(b)].

The irradiation at the below-ablation fluence $F_0 = 0.8F_a$ leads to the formation of a 1.5 nm depth ultra-smooth (roughness $R_a \sim 0.1$ nm) microdimple surrounded by a 3 nm height raised rim and about 1 nm height outer rim seen in Fig. 4(c). It should be noted that the height and depth of observed structures are measured from the baseline of unirradiated intact surface.

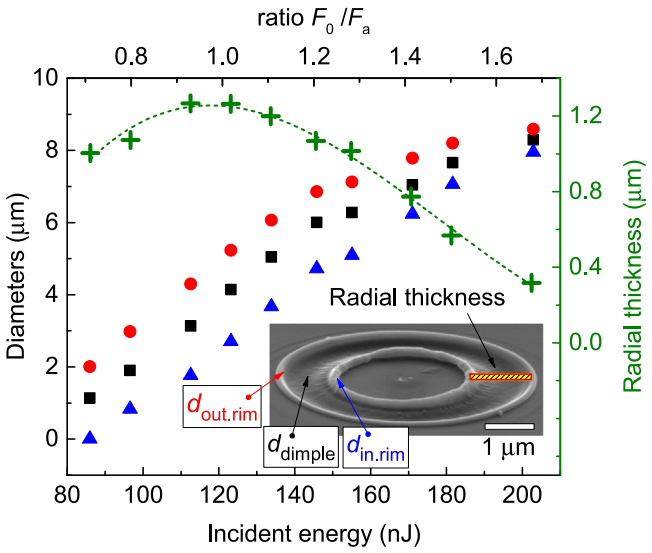

Fig. 5. Diameters of the first dimple (squares) and its radial thickness (crosses), and two surrounding rims (circles and triangles) versus the incident laser energy and fluence ratio F_0/F_a. Definitions of those values are presented in SEM image (inset).

At higher fluences the depth of the microdimple and height of the raised rim are increased [Fig. 4(d)], and at the above-ablation fluence ($F_0 = 1.11F_a$) a 10 nm depth microdimple with the central sub-nanostructured ($R_a \sim 0.5$ nm) area surrounded by a crown-like rim is formed [Fig. 4(e)]. The crown-like rim represents the border of the ablation region of silicon into liquid. No ejection of material is supposed to occur until ablation threshold is exceeded, i.e. the microdimples at fluences below the ablation threshold are formed due to radial redistribution of the molten silicon.

The observed morphology of these structures is similar to those previously produced by infrared (1028 nm) and visible (514 nm) femtosecond laser pulses in other liquids with much different viscosity, such as distilled water and oil [22,24,42]. Amorphization [50], surface-tension and pressure-driven flow of a molten silicon [32], tensile stress induced generation of undersurface defects at below-ablation threshold [51,52] and ablation are supposed to be the main mechanisms in producing such modifications.

It is worth noting that to avoid any damage to the laser-induced structures no ultrasonic cleaning was used, therefore the debris observed at the center of the structures [Fig. 4(c–e)] is supposed to be the product precipitated from glycerol after the collapse of a gas bubble.

3.2. Irradiation with two pulses

Now let us consider the irradiation of the surface of silicon immersed into liquid with two pulses delayed by 200 μs. The spatially-modulated intensity distribution of the second pulse as a result of its diffraction by a bubble in liquid leads to the formation of characteristic annular embossed patterns (so-called circular ripple patterns [24]) on the silicon surface in the form of annular microdimples (or grooves) surrounded by inner and outer rims, see Fig. 4(f–j). It should be noted that the maximum depth of annular microdimples corresponds to the maximum intensity of the incident laser radiation. This follows from a comparison with the single-pulse irradiation mode [Fig. 4(c–e)], where the maximum of the Gaussian intensity distribution corresponds to the maximum depth of the bowl-shaped microdimple. In Section 4 it will be shown that such a modification of the silicon surface relief is associated with the motion of the molten silicon from a hot region to a colder one under a pressure gradient created during the heating of the silicon surface immersed in liquid by a femtosecond laser pulse.

In the case of low intensity (fluence) of the first pulse [Fig. 4(f,g)], the second pulse scatters on a relatively small bubble size which results in the first diffraction ring with minimal diameter. As a result, the melt from the first heated annular zone moving towards the center forms the central peak — hillock (similar to the action of a laser pulse with a doughnut-shaped intensity distribution [15–17]). The hillock is surrounded by a weakly modulated structure in the form of several annular microdimples and rims. In general, with increasing distance from the spot center, the depth of the relief modulation decreases in accordance with the radiation intensity in the diffraction ring pattern (see Section 4).

With increasing laser fluence of the first pulse, the bubble size and diameter of the first diffraction ring are increasing, which results in an increase in the diameter of the first annular microdimple (groove). Therefore, instead of the central peak [Fig. 4(f,g)], a doughnut-shaped rim is formed [Fig. 4(h)]. A further increase in fluence [see Fig. 4(i,j)] is accompanied by an increase in the diameter of the annular structures and a decrease in the radial thickness.

This is illustrated in Fig. 5, where the diameter of the first microdimple (that corresponds to the first diffraction ring) and its radial thickness change with incident laser energy. The diameter of the first microdimple seems to be linearly increasing with increasing incident laser energy (or ratio F/F_a) in the range $[0.7–1.2]F_a$. In the range $[1.2–1.8]F_a$, the growth of the microdimple's diameter slows down. This may be due to slower bubble growth when its size becomes commensurate with the diameter of the laser spot (see Section 4.1). With increasing laser energy, the radial thickness of the microdimple slightly increases in the $[0.7–1]F_a$ range and then decreases three times from the maximum value.

At a fluence of $F_0 = 0.71F_a$ a pattern with a central hillock is produced [Fig. 4(g)], however its height is increased up to 170 nm (as compared with a 100 nm height hillock in [Fig. 4(f)]), and the hillock is surrounded by a distinct annular 16-nm-depth microdimple and 9-nm-height rim. The height of the outer rims in both cases is around 11 nm.

At a fluence of $F_0 = 0.8F_a$ there is a doughnut-shaped rim with an average height of 170 nm surrounded by the first annular 40-nm-depth microdimple, 35-nm-height rim and the second 4-nm-depth microdimple [Fig. 4(h)]. The height of the outer rim is increased to 23 nm. The surface level at the center appears to be unchanged.

At a fluence of $F_0 = 1.02F_a$ an annular microdimple of 70 nm depth with similar in morphology inner and outer doughnut-shaped rims of the average height of 170 and 100 nm, respectively, is formed [Fig. 4(i)]. At a fluence of $F_0 = 1.11F_a$ the annular microdimple depth reaches 80 nm, while a rim height could be as high as 230 nm.

It is worth noting that at high fluences [Fig. 4(h–j)] the surface morphology at the center remains intact after the second pulse interaction, which is possibly due to the screening effect of the bubble. The fact is confirmed by the AFM analysis showing at the center the same morphology generated by the first pulse (see "comparison panel" in Fig. 4). The SEM images made at angle reveal that the highest rims are elevated above the surface similar to a "frozen incoming wave", that will be also demonstrated in TEM images.

Generally, according to the AFM analysis, the central hillocks and doughnut-shaped rims are protruded to a height on the order of 100–230 nm, while a depth of microdimples reaches only up to 80 nm.

3.3. Reproducibility

As shown in Fig. 6, notwithstanding the complexity of the processes involved in producing annular embossed patterns upon irradiation with two pulses under liquid environment, i.e. generation of a bubble by the first pulse and diffraction of the second pulse by the bubble, these surface structures are observed to be formed with high reproducibility, indicating that the process is governed only by the accuracy of deposited laser energy determined by pulse-to-pulse stability of the laser.

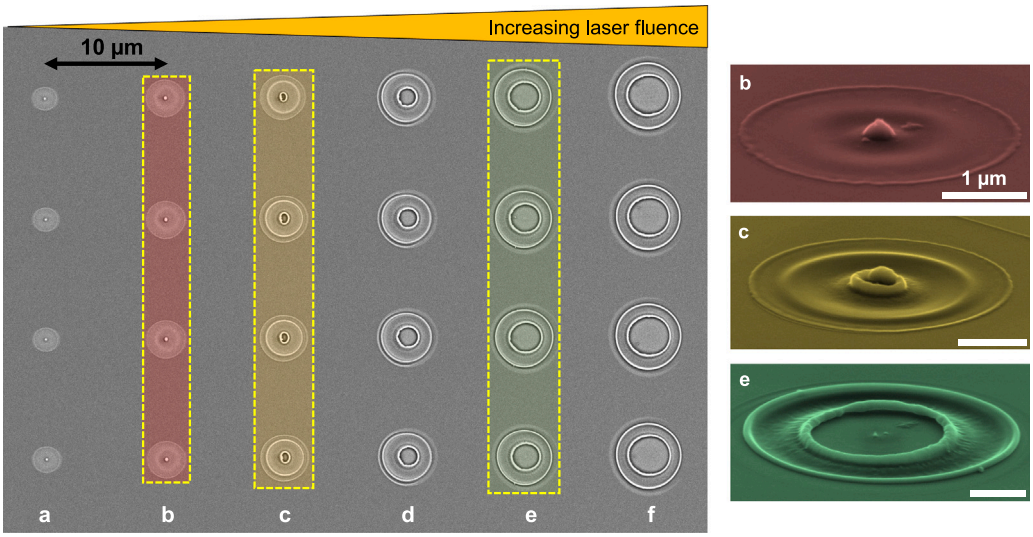

Fig. 6. SEM images demonstrating high reproducibility of the annular embossed patterns produced by the irradiation at 1028 nm in glycerol with two laser pulses delayed by 200 μs in the fluence range F_0 = [0.27–0.49] J/cm^2: (a) $F_0/F_a = 0.62$, (b) $F_0/F_a = 0.71$, (c) $F_0/F_a = 0.8$, (d) $F_0/F_a = 0.93$, (e) $F_0/F_a = 1.02$, (f) $F_0/F_a = 1.11$.

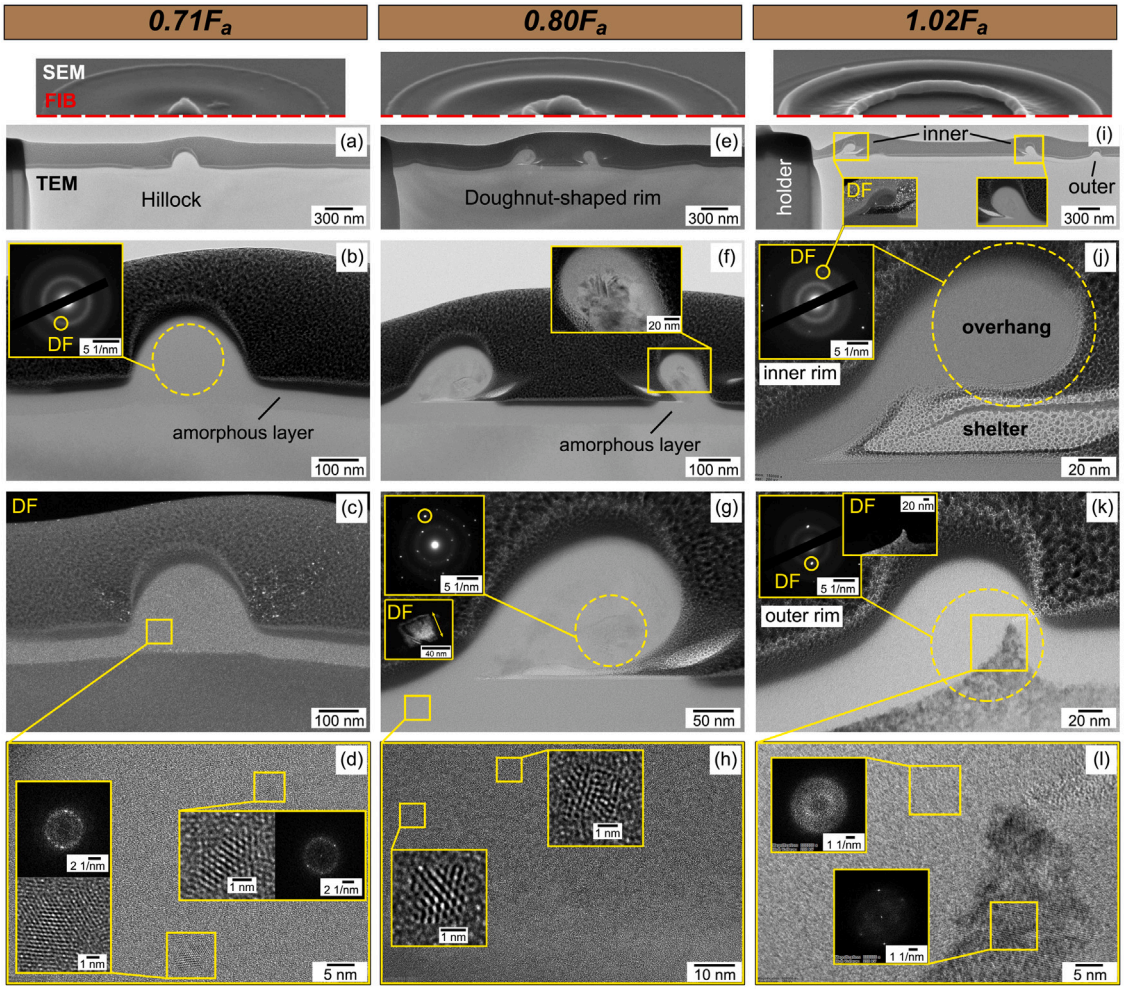

Fig. 7. TEM images of cross-sections of annular embossed patterns produced on the silicon surface in glycerol with two pulses delayed by 200 μs at fluences of (a–d) $F_0 = 0.71F_a$, (e–h) $F_0 = 0.8F_a$, and (i–l) $F_0 = 1.02F_a$.

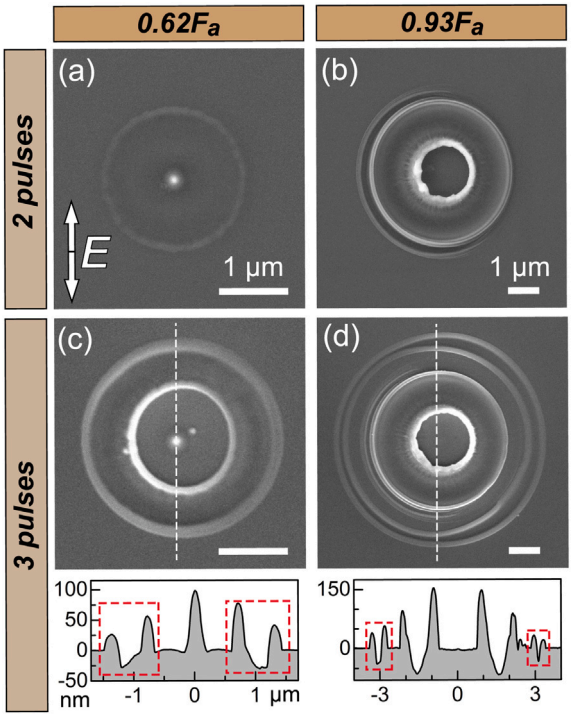

Fig. 8. The annular embossed patterns on the silicon surface after irradiation with two (a–b) and three (c–d) laser pulses at 1028 nm delayed by 200 μs each with various fluence ($0.62F_a$ and $0.93F_a$) in glycerol. The SEM images and AFM cross-sections are shown. The white dashed lines show the location of the cross-sections. The white arrow shows the direction of laser polarization.

3.4. TEM analysis

The surface relief and undersurface structure of the annular embossed patterns produced with the irradiation of the silicon sample in glycerol with two pulses delayed by 200 μs at the wavelength of 1028 nm at fluences $0.71F_a$, $0.8F_a$ and $1.02F_a$ were studied in detail by transmission electron microscopy (TEM) (Fig. 7). To determine the degree of crystallinity of the modified surface layer the electron diffraction patterns, dark field (DF) images of certain reflections, and high-resolution TEM (HRTEM) images were investigated.

All the studied structures obtained at fluences in range of $[0.71–1.02]F_a$ are characterized by the presence of a surface layer consisted of amorphous silicon, the thickness of which increases from 50 nm presented in Fig. 7(a–c) to 90 nm in Fig. 7(i–k), respectively. In the amorphous layer, there was observed a small number of inclusions of randomly arranged disordered silicon nanocrystallites ranging in size from 1 to 5 nm. For all the studied annular embossed patterns the contrast between the upper (amorphous) layer and the underlying part (combination of fine-crystalline, single-crystal and amorphous phases) remains approximately the same over the length of the irradiated part of the sample. There were observed no bright areas in the images, which indicates the absence of subsurface voids. The protruding parts of the structures also consist predominantly from the amorphous phase, however in some cases, inclusions of nanocrystals with a size of several tens of nanometers may be present [Fig. 7(f)].

It should be noted that the thickness of the amorphous layer in our experiments slightly exceeds the thickness of the amorphous layer in experiments carried out in air at similar laser pulse fluences [50,53–55]. A possible reason for this is the additional cooling of the surface during the formation of a vapor bubble [32]. At the same time, the role of the effect of liquid on the amorphization of the silicon surface requires more detailed studies, which is beyond the scope of this work.

At a minimum fluence of $F_0 = 0.71F_a$, a bell-shaped hillock shown in Fig. 7(a–c) with the height of about 170 nm is formed in the center of structure. Such a hillock is entirely made of amorphous silicon. This is evidenced by the electron diffraction pattern, which consists of wide diffuse rings illustrated by inset in Fig. 7(b). The dark-field TEM image taken in the first bright diffuse ring of the electron diffraction pattern is shown in Fig. 7(c).

At higher fluences, the doughnut-shaped rims have an asymmetric drop-like shape, indicating the direction of melt motion, see Section 4. At the same time, these doughnut-shaped rims can either lie on the surface [Fig. 7(g)] or hang over it [Fig. 7(j)], thereby creating an above-surface cavity-shelter. For example, the inner doughnut-shaped rim in Fig. 7(j) hangs over the surface in the form of a drop ("overhang" 110 × 160 nm) on a stem about 30–35 nm thick. The shelter under it has a height of up to 55 nm and a width of up to 200 nm. The shelter is represented by a light area in the bright-field image and a black area in the dark-field image (inset in Fig. 7(i)), since it was not completely filled with Pt during the deposition of the protective layer.

The outer rim shown in Fig. 7(k) is of smaller height, comparing to the central doughnut-shaped rim, and is less asymmetrical. It consists of separated amorphous and crystalline phases. The electron diffraction pattern contains bright wide diffuse rings characteristic of the amorphous phase and several bright reflections of the crystalline phase. The dark-field TEM image taken in the reflection marked with a circle is shown in the inset in Fig. 7(k). These reflections on the electron diffraction pattern correspond to the fine-crystalline phase.

The structure of the material inside the doughnut-shaped rim may not be uniform [Fig. 7(f)]. The corresponding diffraction pattern in Fig. 7(g) is a superposition of wide diffuse rings characteristic of the amorphous phase and bright point reflections characteristic to the crystalline phase. A dark-field TEM image taken in reflection illustrates the presence of a 40–50 nm crystalline region inside the rim [inset in Fig. 7(g)].

To detect the presence of nanocrystallites several nanometers in size inside the amorphous phase, HRTEM images were obtained. In the inserts of Fig. 7(d,h) one can see the HRTEM images of several regions, which show that among the labyrinth pattern characteristic of an amorphous matrix, there are randomly arranged nanocrystallites (areas containing parallel atomic planes) ranging in size from 2 to 6 nm.

3.5. Irradiation with three pulses

The annular embossed patterns after irradiation with two and three pulses are shown in Fig. 8(a, b) and Fig. 8(c,d), respectively (all laser pulses are delayed by 200 μs). As it could be seen from Fig. 8, the action of the third pulse results in the formation of a new annular microdimple at the periphery (these structures are marked by red dashed rectangles on the AFM profiles). This behavior can be explained by an increase in the size of the bubble formed upon irradiation with the second pulse, compared to that formed after exposure to the first pulse. This increase can be associated with an increased absorption coefficient of the modified silicon surface, as well as due to the coalescence of the first bubble with the next one. Note that hillocks or doughnut-shaped ring structures produced upon irradiation with the second pulse [Fig. 8(c–d)] remain intact upon irradiation with the third pulse as a result of the shielding effect of the central region by a bigger bubble.

3.6. Effect of laser wavelength

The effect of laser wavelength (1028 and 514 nm) on annular embossed patterns was also investigated and is illustrated in Fig. 9 which shows their angled SEM images and the corresponding AFM cross-sections. The silicon surface immersed into viscous liquid was irradiated with two pulses delayed by 200 μs at similar fluences. Note that in Fig. 9 bar lines in angled SEM images are nearly the same and X-axis scales in AFM cross-sections are identical for groups (a,c) and

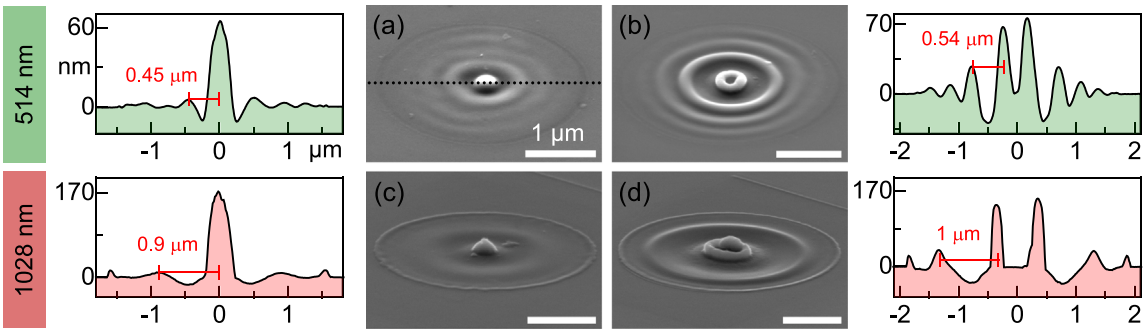

Fig. 9. Effect of laser wavelength on spatial period and surface relief modulation magnitude of annular embossed patterns in viscous liquid. SEM images and AFM cross sections: (a) $0.76F_a$ and (b) $0.88F_a$ at 514 nm, (c) $0.71F_a$ and (d) $0.80F_a$ at 1028 nm laser wavelength. The dotted line indicates the cross-section location in AFM scan.

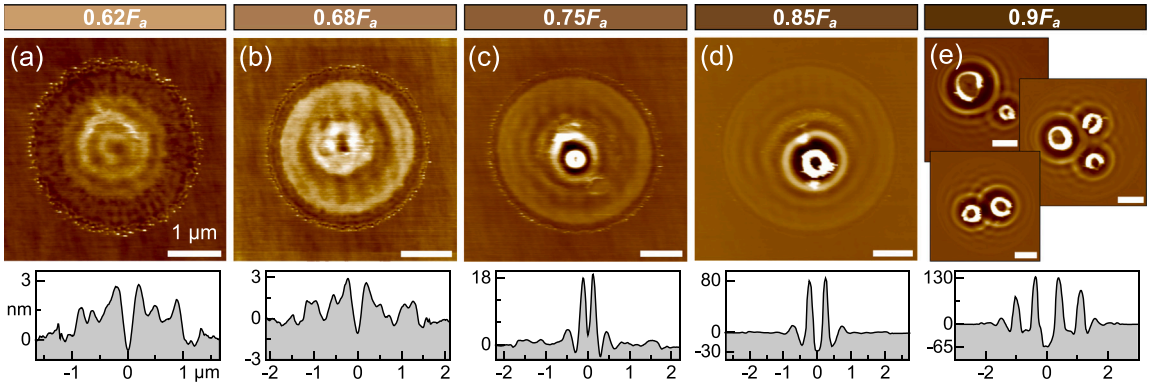

Fig. 10. The annular embossed patterns produced by two pulses delayed by 200 μs at a wavelength of 514 nm in distilled water. The AFM scans and the corresponding cross-sections are shown.

(b,d) for ease of comparison. As it could be seen from the images, in general, halving the incident laser wavelength from 1028 nm to 514 nm results in doubling the modulation frequency of the surface relief of the annular embossed patterns. For example, the radial thickness of the first annular microdimple, which corresponds to the first diffraction ring, changes from [0.45–0.54] μm at the wavelength of 514 nm to [0.9–1] μm at the wavelength of 1028 nm. At the same time, the maximum height of the structures like hillocks and doughnut-shaped rims increases from 60–70 nm at the wavelength of 514 nm to 160–170 nm at the wavelength of 1028 nm, which could be related to the increasing radial thickness (spatial period) of diffraction rings and the corresponding increase in amount of molten silicon to redistribute.

3.7. Effect of liquid: irradiation with two pulses

In viscous liquids such as glycerol (this work) and oil [24] in a wide range of fluences F_0/F_a = [0.6–1.1] we observed well-reproducible annular embossed patterns with a center of symmetry located on the laser beam axis, which indicates stable generation of a single gas bubble (Fig. 6). At the same time, changing viscous liquids to a distilled water results in chaotically-located annular embossed patterns which is apparently the result of the diffraction of the second pulse by several so-called persistent (or secondary) gas bubbles [Fig. 10(e)] that are produced after collapse of the primary bubble [56]. Moreover, as opposed to irradiation in viscous liquids, in water there is a maximum of radiation intensity on the beam axis, as evidenced by the presence of the central microdimple several tens of nanometers deep [Fig. 10(c–e)], that could be related to the bubble transmission of paraxial laser rays (refraction), or due to the bubble position at some distance above the surface thus allowing diffracting rays irradiate the central spot of geometrical shadow. We do not consider that the observed structures are due to the laser beam filamentation in water [57,58], because the absence of filamentation has been evidenced by the axial (or circular) symmetry of the laser-produced structures upon single-pulse irradiation in a wide range of fluences [42].

It is worth noting that due to close similarity of the annular patterns shown in Fig. 10(e), which are formed as a result of diffraction of the second pulse by three separate bubbles, with those patterns previously observed in Refs. [34–37] upon irradiation with a single pulse, we suppose the diffraction by several pre-existing bubbles had also taken place in these studies. The close similarity is expressed in spatial period of patterns being comparable with the exciting laser wavelength and the surface relief modulation being about several tens of nanometers.

Summarizing the results of experiments described above, the following conclusions can be made. The action of a pair of tightly focused ultrashort laser pulses on silicon in liquid in a certain range of laser fluences results in the formation of annular embossed patterns of various configurations on the surface. With a fixed delay between the two pulses, the configuration of surface patterns can be easily controlled solely by varying the pulse energy. The modulation of the modified surface relief in the case of irradiation with two pulses, reaching hundreds of nanometers, is more than an order of magnitude higher than the modulation upon irradiation with a single pulse of the same energy. In this case, annular microdimples on the surface correspond to the maximum radiation intensity. The mechanism of formation of annular embossed patterns is due to the diffraction of the second pulse by a gas microbubble formed in liquid after heating the silicon surface by the first pulse.

The formation of a bubble in liquid upon irradiation with the first pulse and diffraction of the second pulse by the bubble, in our opinion, is unambiguously evidenced by the following results: (1) ring shape of the formed structures while a laser pulse with Gaussian intensity profile was used; (2) an increase in the spatial frequency of the annular embossed patterns (and, accordingly, diffraction rings) with a decrease in the wavelength of laser radiation; (3) screening of the central part of the sample's surface by a bubble with increasing fluence; (4) the

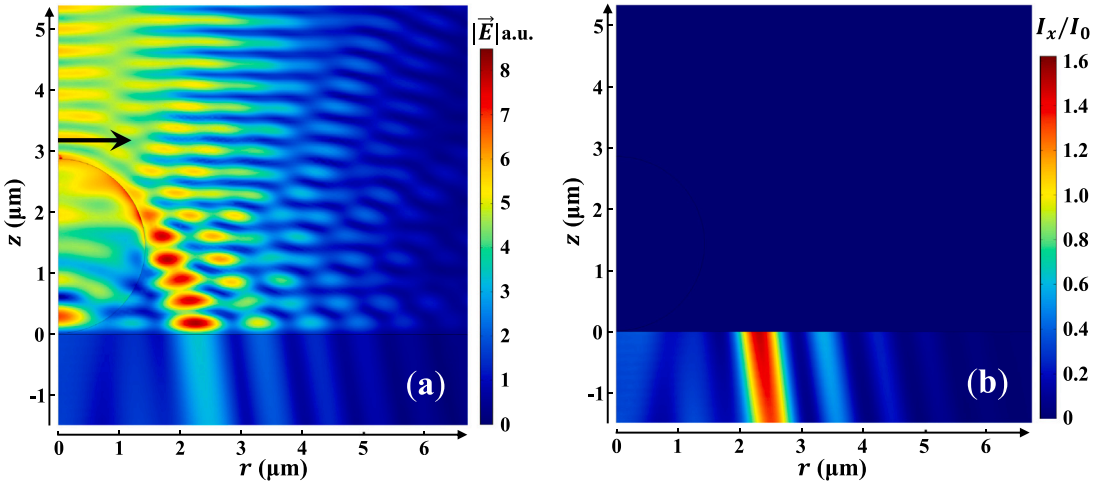

Fig. 11. Diffraction of the second pulse calculated at bubble parameters $R = d = 1.42\,\mu m$. (a) Electric field modulus distribution (in arbitrary units) in the plane passing through the incident beam axis (normal to the silicon surface) and parallel to the incident beam polarization. The big black arrow indicates electric field polarization of the beam. (b) Normalized electric field intensity $I_x(r, z)/I_0$ in silicon in the same plane (shown only in silicon, not in liquid nor bubble).

formation of additional annular microdimples upon irradiation with three pulses; (5) the formation of multiple bubbles in a low viscosity medium.

4. Diffraction modeling and MD simulation

4.1. Diffraction modeling

To clarify the formation mechanisms of the annular embossed patterns on the silicon surface immersed into liquid after irradiation with two laser pulses delayed by 200 μs, we performed numerical simulations of the diffraction of a laser pulse by a bubble in liquid. The simulations were performed using Comsol Multiphysics (finite element method). The incidence of a laser beam with a Gaussian intensity distribution on the silicon surface was simulated in an axisymmetric configuration for a clockwise and counter clockwise circularly polarized Gaussian beams. Then, using these two solutions for circularly polarized Gaussian beams, a solution was constructed for the linearly polarized Gaussian beam used in the experiment.

The numerical simulations were performed for two cases. The first case corresponded to irradiation of a flat unmodified silicon surface in homogeneous glycerol with the first linearly polarized laser pulse. The second case corresponded to irradiation of the silicon surface with the second laser pulse. In this case, a gas bubble (centered on the beam axis) in the form of a sphere or a truncated sphere with a radius R and a distance d from the silicon surface to the sphere center was located above the silicon surface in glycerol. Here for $d \geqslant R$, the bubble is an ideal sphere, whereas for $0 < d < R$, it is a truncated sphere, adjacent to the flat silicon surface.

In both cases, we assumed that silicon occupied a half-space. The first pulse illuminated a flat smooth silicon surface. Upon incidence of the second pulse, the silicon surface could have a nonplanar relief. However, we assumed that the silicon surface relief formed after the first pulse had a weak effect on the second pulse propagation. As shown in Fig. 4(a–e), the modulation amplitude of the silicon surface profile after the first pulse irradiation did not exceed 10 nm in the range of the used laser fluence.

In the electromagnetic simulation of pulse propagation in silicon, we do not consider nonlinear optical effects in silicon. The silicon refractive index is $n_{Si} = 3.566 + 3 \cdot 10^{-4} i$ [59] at the laser wavelength in vacuum $\lambda = 1028$ nm. The glycerol refractive index is $n_{gl} = 1.4633$ and the refractive index of gas in the bubble is $n_b = 1$.

From the first pulse irradiation simulation, the distribution of the incident beam electric field intensity $|\vec{E}|^2$ in silicon was obtained as a function of the pulse energy. The maximum electric field intensity $I_0(F_0) = |\vec{E}(r = 0, z = -0)|^2$ in silicon (on the beam axis, just near the silicon/glycerol interface) was determined for a given pulse fluence F_0. Subsequently, the quantity $I_0(F_0)$ is used to normalize the spatial redistribution of the electric field intensity in silicon for the second pulse.

From the second pulse irradiation simulation, in the presence of a gas bubble in glycerol, the electric field intensity distribution $I(r, F_0) = |\vec{E}|^2$ in silicon was obtained as a function of the radial coordinate r (for some fixed value of the coordinate z normal to the silicon surface (see Fig. 11), inside silicon). Below we consider the function $I(r, F_0)/I_0(F_0)$ as a function of r characterizing the redistribution of the electric field intensity in silicon due to diffraction by the bubble. Obviously, in the limit of low absorption in silicon (Im $n_{Si} \ll$ Re n_{Si}), the function $I(r, F_0)/I_0(F_0)$ is independent on the Im n_{Si} used in simulations. In addition, possible optical nonlinearities in silicon during the second pulse incidence weakly affect the function $I(r, F_0)/I_0(F_0)$ (at small depth z in silicon) determined primarily by the bubble characteristics R and d.

As an example, in Fig. 11(a) the electric field modulus distribution is shown in the plane passing through the incident beam axis (normal to the silicon surface) and parallel to the incident beam E-field polarization for $R = d = 1.42\,\mu m$. And in Fig. 11(b), the distribution of I_x/I_0 in silicon is shown in the same plane and for the same R and d (the subscript x denotes that the distribution is in the plane parallel to the incident beam polarization).

Depending on the values of R and d, the radial positions r_x and r_y of the main maxima of $I(r)/I_0$ at a depth of 20 nm in silicon were determined. The position r_x corresponds to the radial position of the main maximum of $I_x(r)/I_0$ (in the direction along the polarization of the incident beam), the position r_y — to the radial position of the main maximum of $I_y(r)/I_0$ (in the direction perpendicular to the incident beam polarization). We chose the depth of 20 nm because it is of the order of depth of annular dimples formed in silicon. On the other hand, the radial positions of maxima of $I(r)/I_0$ slowly vary with z (see e.g. Fig. 11(b)). Thus, the choice of 20 nm is rather arbitrary.

It should be noted that the positions r_x and r_y are different in general because the incident beam is linearly polarized and diffraction rings are not strictly circular on the silicon surface. This noncircularity of diffraction rings results in slight (no more than 8%) noncircularity of the observed dimples on the silicon surface (see Fig. 6 and surface profiles in the bottom of Fig. 4).

Based on the experimental radial positions of the annular minima of the silicon surface profile after irradiation with the second pulse,

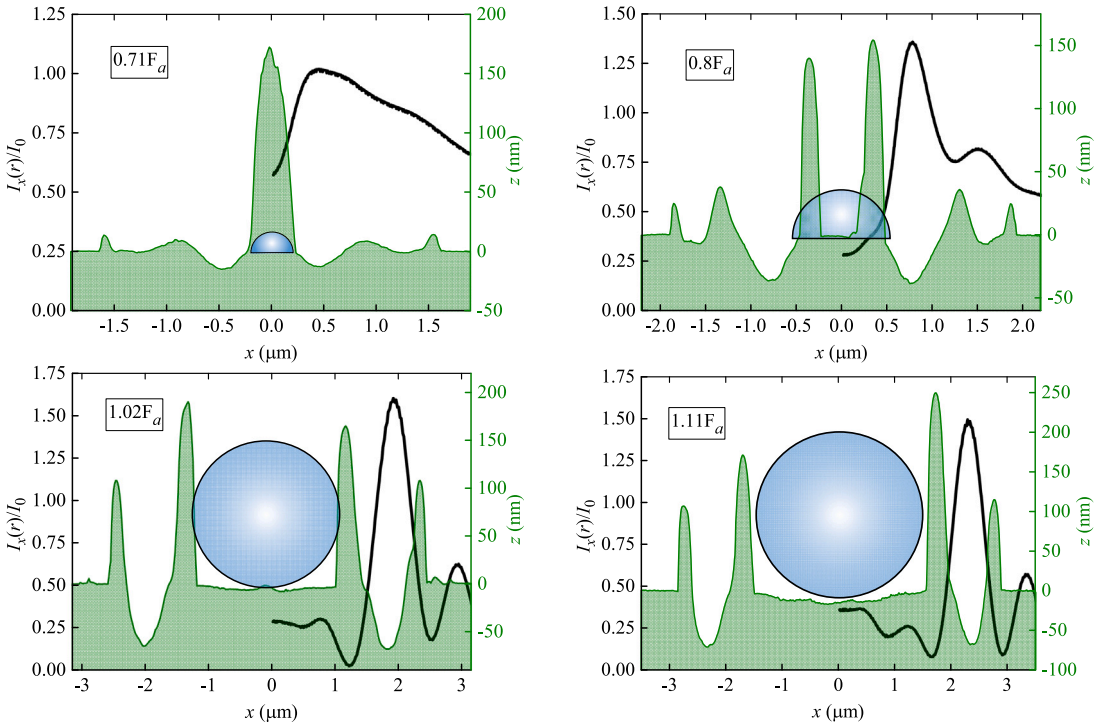

Fig. 12. Comparison of simulated normalized intensity distributions $I_x(r)/I_0$ in silicon for the second pulse (black curve) with measured (AFM) reliefs of a modified silicon surface (green curve) for different F_0/F_a in the x-direction (parallel to the incident beam polarization). As examples, for $0.71F_a$ and $0.8F_a$ we show intensity distributions for the limiting case of $d = 0$ and the corresponding R determined for these fluences, and for $1.02F_a$ and $1.11F_a$ we present intensity distributions for the case of $R = d$. In addition, the bubbles with the determined parameters R and d are shown (bubble size is shown according to the horizontal size scale). Notice that the surface reliefs are in nanometers along Z-axis, while the bubbles's dimensions are in micrometers.

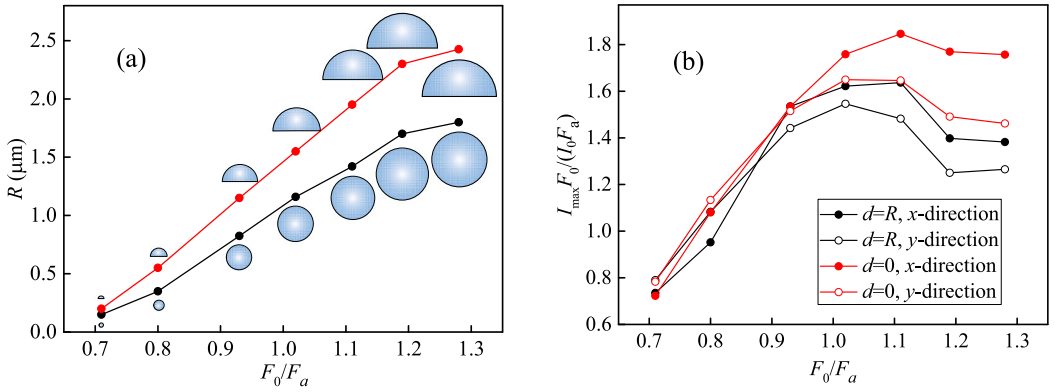

Fig. 13. (a) The bubble radius R as a function of the pulse fluence F_0/F_a. The black curve corresponds to the full-sphere case $d = R$ and the red curve — to the hemisphere case $d = 0$. In addition, for each F_0/F_a the bubbles' shapes and sizes are shown (the displayed sizes are proportional to real sizes, but not related to the graph scales). (b) Dependence of the maximum (along the radial coordinate) normalized electric field intensity $I_{\max}F_0/(I_0F_a)$ in silicon at the depth of 20 nm on the pulse fluence F_0/F_a. The black curves correspond to the $d = R$ case and the red curves — to the $d = 0$ case. The filled-dots-curves correspond to the maxima of the function $I_x(r)F_0/(I_0F_a)$, whereas the void-dots-curves correspond to the maxima of $I_y(r)F_0/(I_0F_a)$.

depending on the pulse energy (see Fig. 5), the values of R and d are determined (for each pulse fluence F_0) so that the radial positions of the experimental minima of the surface profile coincide with r_x or r_y. The coincidence of positions of surface profile minima and intensity maxima results from experiments with single-pulse silicon surface modification (see Fig. 4). According to [32] and the next Section 4.2, the silicon surface heating by an ultrashort laser pulse in liquid leads to silicon melting and melt outflow from the heated area to the periphery resulting in a dimple formation.

However, the coincidence of radial positions of profile minima and intensity maxima does not allow to determine the R and d parameters unambiguously. Therefore, we considered two limiting cases: a spherical bubble touching the silicon surface ($d = R$) and a hemispherical bubble ($d = 0$). According to PLAL experiments on metal samples carried out using picosecond [26–28] and nanosecond [60–66] pulses, a primary bubble normally has a hemispherical form. In our case, on the one hand, as the unirradiated silicon surface is well wetted by glycerol (contact angle is around 45 degrees), the bubble in opposite should have nearly a spherical form. On the other hand, the irradiation of silicon surface by the first pulse can change the surface roughness/chemistry which in turn can change the bubble contact angle resulting in the formation of a hemispherical bubble. For information about the actual shape and spatial position of the bubble further research is needed that is beyond the scope of this work. In addition, it should be noted that in our experiment the laser radiation

was oppositely directed to the gravitation forces (see Fig. 2), therefore there was no buoyancy force tended to bring the bubble farther from the silicon surface.

Fig. 12 shows the experimental profiles of the modified silicon surface (upon irradiation with the two pulses) together with the simulated intensity distributions $I_x(r)/I_0$ in the diffraction patterns for various fluences.

The determined bubble radii R for various pulse fluences F_0/F_a are shown for two limiting cases of $d = R$ and $d = 0$ in Fig. 13(a). The corresponding functions $(I_x(r_x)/I_0)(F_0/F_a)$ and $(I_y(r_y)/I_0)(F_0/F_a)$ of the argument F_0/F_a are presented in Fig. 13(b). The values of R and d were determined from the requirement of coincidence of r_x and the position of surface profile minimum in the x-direction parallel to the beam polarization. For the determined pairs of R and d values, r_x and r_y differ by less than 5%. Therefore, the choice of e.g. the y-direction for matching experimental and simulation data instead of the x-direction would result in nearly the same pairs of R and d values determined. From Fig. 13(b), we can infer, that in the considered range of fluences (except $F_0/F_a = 0.71$) the absorption is strong enough for ablation to occur ($I_{\max}F_0/(I_0F_a) > 1$), although even at smaller fluences surface relief modification is possible (compare the surface modification F_{mod} and ablation F_a thresholds in Table 1). From Fig. 13(a), the monotonic increase of R with the increase of F_0/F_a is evident, which can be explained by the increasing heating of silicon during the irradiation with the first pulse and a larger volume of evaporated glycerol at higher fluences F_0/F_a.

Thus, from matching experimental data with simulated field intensity distributions in the fluence range of $[0.71–1.28]F_a$, we conclude that the bubble radius R increases monotonically from 0.15 to 1.8 μm (or from 0.2 to 2.4 μm for $d = 0$) with the increase of F_0. The maximal increase of the electric field intensity in silicon compared to the case without a bubble reaches $I(r)/I_0 = 1.65$ (at $F_0/F_a = 0.93$) for the case of a full sphere and $I(r)/I_0 = 1.72$ (at $F_0/F_a = 1.02$) for the case of a hemisphere due to diffraction on the bubble. For $F_0/F_a > 1.02$, however, $I_{\max}/I_0$ becomes smaller, because the bubble size becomes of the order of the incident beam width shielding silicon from the central part of the beam.

4.2. MD simulation

To explore the physical mechanisms leading to formation of the annular grooves surrounded by two rims after heating by tightly focused light diffracted by a bubble, we have applied the direct atomistic simulation using molecular dynamics (MD) method. In contrast to hydrodynamic approaches it naturally involves a variety of processes such as melting, crystallization, cavitation and ablation, whose develop over a wide time scale from femtoseconds to microseconds, and also are guided by surface tension. However, the size of focal spot, as well as the complexity of interatomic interaction in glycerol and silicon, in particular the interaction between a Si atom and a glycerol molecule, do not allow to perform MD simulations under experimental conditions. Therefore, MD simulations were performed for relatively small systems (many times smaller than the experimental sizes), and for a pair of substances with similar mechanical parameters, namely density and speed of sound. Our goal was not to quantitatively-accurately reproduce the physical phenomena in experimental conditions, but to discover the possible physical processes responsible for the formation of the observed surface structures.

Glycerol is represented by the atomic model of water (molecule as a point particle) with the EAM potential [67], and silicon by the aluminum model with the EAM potential [68]. The masses of glycerol and silicon “atoms” are chosen to match the densities and acoustic impedances of these materials at normal conditions. The interparticle interaction between those glycerol and silicon ”atoms” is described by the Lennard-Jones potential with the small depth of potential well $\varepsilon/k_B = 113$K as between oxygen molecules, and with the well minimum

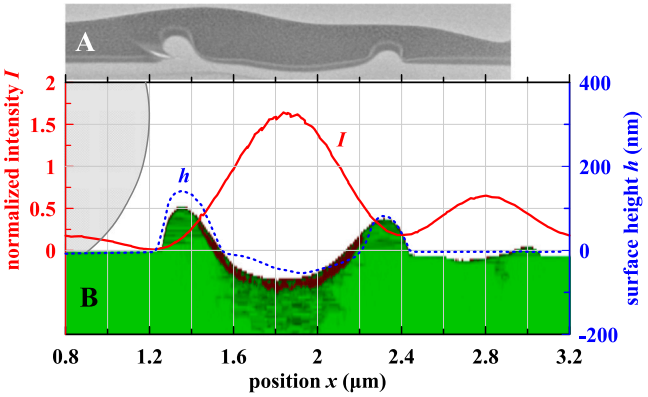

Fig. 14. Groove surrounded by two rims after crystallization of molten silicon. Laser heating is done by a calculated diffraction intensity (red line) around a bubble with $R = 1.2$ μm (gray circle) sitting on the surface at $d = 0.8$ μm. Blue dashed line shows the measured surface height $h(x)$. The vertical scale of $h(x)$ is half of the horizontal scale. (A) TEM image of the cross-section of the annular groove formed on the silicon surface upon irradiation with two pulses at $F_0 = 1.02F_a$. (B) Map of center-symmetry parameter across a straight groove obtained in MD simulation of 2D sample at $t \approx 600$ ps after planar heating. Solid is colored by green, liquid by red. Fast freezing of melt generates many defects (dark green). Only silicon is shown.

position equal to the sum of Van der Waals radii of silicon atom (0.21 nm) and oxygen atom (0.152 nm).

Two samples were prepared — for 2D simulations of heating with a planar intensity profile obtained after diffraction modeling described in the previous section, and for 3D simulations of heating with an annular light intensity distribution with a single annular diffraction peak around the bubble. A $L_z = 200$ nm thick layer of glycerol covers a 300 nm silicon layer in the both samples, with the upper glycerol boundary and the lower silicon boundary being free and the vapor density above them being nearly zero. The bulk sample has transverse dimensions $L_x = L_y = 200$ nm, and the planar sample has $L_x = 800$ nm on the horizontal axis, but its size on the y axis is small $L_y = 10$ nm. Periodic boundary conditions are imposed on all three axes. In total there are about 143×10^6 silicon atoms and 52×10^6 glycerol ”atoms” in the planar sample, and 5 times more in the bulk sample.

Before laser heating of silicon, the MD samples are brought to mechanical and thermodynamic equilibrium at $p \approx 0$ and $T_0 = 300$K using the Langevin thermostat. The silicon surface in the planar sample is then heated by this thermostat to reach a target temperature field $T(x, z) = (T_s - T_0) * T(x) * T(z) + T_0$ for 2 ps, which is typical of the energy transfer time from the electron to phonon subsystem in aluminum. The depth temperature distribution $T(z)$ is chosen to be Gaussian $T(z) = \exp[-(z/20)^2]$, and the surface distribution $T(x)$ — consisting of a combination of two Gaussian profiles $T(x) = \exp[-((x + 108)/84)^2]+0.3\exp[-((x-108)/70)^2]$, where numerical values in nanometers are used. The given surface profile $T(x)$ is similar in distance between diffraction peaks and their amplitudes to the calculated intensity profile shown by the red line in Fig. 14, but the spatial scale is about 4.4 times smaller than in the experiment. To establish similarity between simulation and experiment, this scaling factor is used to set the heating depth in the MD simulation, and to compare the simulated and experimental silicon surface profiles shown in Fig. 14.

To exclude deceleration of material flow generated by thermal pressure gradient in the XZ plane, the thermostat heating is applied only to the y-velocity components of atoms. Transfer of thermal energy to other translational degrees of freedom proceeds readily by interatomic collisions.

Similarly, the 3D sample is heated to the target temperature field $T(r, z) = (T_s - T_0) * T(r) * T(z) + T_0$, where the radial component $T(r)$ in the silicon surface is given by the Gaussian profile $T(r) = \exp[-((r - 40)/25)^2]$. This spatial temperature distribution corresponds

to a scale factor of 12 when compared with the calculated diffraction field at $0.71F_a$ shown in Fig. 11. This figure also shows a surface profile with a central peak, which we aim to reproduce in our MD simulation. It should be noted here that the maximum surface temperatures T_s in the spatial distributions $T(r,z)$ for $0.71F_a$ and $T(x,z)$ for $1.02F_a$ are chosen so as to reproduce qualitatively the experimental profiles of the modified target surface in Fig. 11.

Fig. 14 shows the results of MD simulations of the planar sample. The modified silicon surface is presented after almost complete crystallization of the melt at $t \approx 600$ ps. The map of center-symmetry order parameter of atoms [69] represents the solid silicon in green and the melt in red. The shallow melting in the second weak diffraction peak does not lead to sizeable surface modifications.

Due to almost isochoric heating of the 20 nm deep surface layer to $T_s \approx 6800$ K, the first most powerful diffraction peak generates a high thermal pressure $P_{max} \approx 20$ GPa in this layer during the first 2 ps. The specified T_s is chosen so that the weaker second diffraction peak cannot create its groove in agreement with the experiment, as can be seen from the measured height $h(r)$ and TEM image in Fig. 14.

Because of the tight focusing, the pressure gradient in the plane of this hot surface layer is established at approximately 0.2 GPa/nm in MD simulation. Despite the fact that the glycerol resists to thermal expansion of the melt, the pressure in the layer gradually dropped by 5 ps. Nevertheless, this time is enough to drive the silicon melt into a flow diverging from the center of diffraction peak, whose velocity reaches $u_{max} \approx 210$ m/s. Subsequently, the melt flows out of the groove by inertia, and is controlled by the weaker forces of surface tension and viscosity.

Rapid cooling of the hot melt leads to its gradual solidification starting from the depth of sample and the edges of melted groove. The crystallization rate significantly accelerates after 350 ps, when the melt temperature drops almost everywhere below the melting point, and is determined by the degree of melt supercooling. The near-final profile of target surface shown in Fig. 14 is obtained after solidification of the diverging flow in the form of two rims surrounding the groove. The heights of these rims should be the same in the planar heating, but the counteraction of the second weak diffraction peak makes the right rim slightly lower and wider than the left one. The difference in heights observed in the experiment is explained by the circular geometry of the diffraction field around the bubble symmetry axis. Because of this, the converging and diverging radial flows from the heated zone are formed, which result in an annular groove with inner and outer rims of different radius. Their radii in Fig. 14 are approximately 1.36 μm and 2.32 μm, respectively, which gives the expected height ratio of 1.71, provided the mass fluxes in the both flows are equal, and the frozen rims are the same width. The measured heights of the rims relative to the original target surface 146 and 86 nm give almost the same ratio of 1.7.

The evolution of the silicon surface obtained in a 3D simulation of circular heating by the first diffraction peak is shown in Fig. 15. The maps of the local order parameter in a thin section of the silicon sample in the XZ plane are shown. Immediately after 2 ps of heating, a cylindrical melt groove forms around the bubble axis of symmetry, while the central island under the bubble remaining solid in the beginning. The high pressure in the groove produces expansion of the melt and generates a strong toroidal (doughnut-shaped) shock wave (SW) in the solid silicon, and a weak SW in the glycerol. Part of the toroidal shock front converges from the circular groove toward the central axis. The pressure gradient in the target plane causes as usual the radial oscillations of the melt inside the groove, but soon such symmetric motion experiences a radial perturbation, resulting in a capillary wave diverging from the central axis, as shown in a snapshot at $t = 67$ ps in Fig. 15. The reason of such surface perturbation is a diverging SW arising after reflection of the converging part of toroidal SW from the central axis. This diverging SW accelerates radially the melt, which produces a radially diverging surface wave.

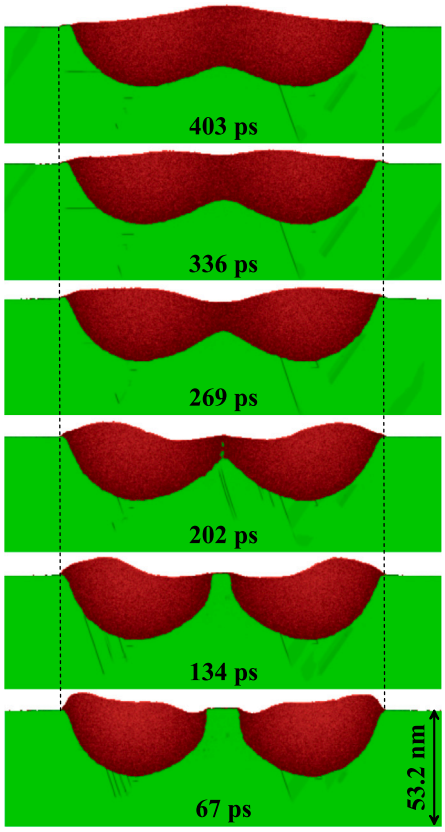

Fig. 15. Radial capillary wave on silicon, melted in a ring-like pool (groove) under a bubble, obtained in MD simulation at $F_0 = 0.71F_a$. Cross-sections through the central axis show evolution of central symmetry parameter, where red color represents liquid and green — solid material. At early times the melt and pool surface is perturbed by a diverging radial shock wave in silicon. As a result, the melt is pushed radially from the axis as seen at $t = 67$ ps. After reflection from an outer bank of pool the capillary wave is turned to the center, where the converging wave forms a bump seen at 403 ps. Glycerol is not shown.

Next, this surface wave (including the melt beneath the surface) moves toward the outer edge of the groove, as shown in snapshots at 202 and 269 ps. By the last time, the central island has completely melted, and the groove has become a round pool. Then the wave is reflected from the pool edge and begins to converge to the pool center, as seen in snapshots at 336 and 403 ps. At the last moment, the wave profile forms a peak at the center of pool. We think that the described process may lead to the formation of a central hillock in Fig. 4(g) at $F_0 = 0.71F_a$ if the freezing time is consistent with the focusing time of capillary wave in the center. It is also possible that the fast decrease in pool radius due to freezing increases the height of wave profile, and growth of the central hillock occurs gradually as it freezes after a few oscillations of the melt surface. Complete freezing would require several nanoseconds of MD simulations, which is too long to perform for an admissible wall-clock time.

5. Conclusion

In summary, the paper presents the results of experimental and theoretical studies of the formation of annular embossed patterns on the surface of single-crystal silicon in two liquids with different viscosities (glycerol, water) after exposure to one, two or three ultrashort laser pulses following with a certain time delay. Silicon surface heating by a tightly focused laser pulse with an intensity near the melting and ablation thresholds leads to the formation of a microscale gas bubble localized near the surface. If the delay between laser pulses is less than

the bubble collapse time, the diffraction of a newly incident pulse by the bubble leads to the formation of annular embossed patterns on the surface. This effect is observed in a limited range of fluences near the ablation threshold. The fluence range has a lower limit associated with the silicon melting threshold (near half the ablation threshold) and an upper limit at which the bubble diameter becomes comparable with the laser focal spot and starts shielding the incident laser radiation (nearly two times the ablation threshold).

Varying the fluence of laser pulses allows to fabricate annular embossed patterns of various configurations, including the central hillock or doughnut-shaped rims surrounded by annular microdimples (grooves). It is important that although the peak intensity increases by less than a factor of 2 when irradiated with diffraction ring patterns, an unusually large modulation of the surface relief is observed. It reaches several hundreds of nanometers, which is more than an order of magnitude higher than the surface modulation in the case of exposure to a single laser pulse with a Gaussian intensity distribution.

The spatial frequency of the surface relief modulation is two times higher at the second harmonic (514 nm) as compared to the fundamental laser wavelength (1028 nm). The irradiation with three laser pulses results in the formation of additional annular microdimple on the periphery. Obviously, this is due to the larger absorption coefficient of the modified surface, and, accordingly, the bigger size of the bubble generated upon irradiation with the second pulse.

In the fluence range $[0.6–1.1]F_a$ in the viscous liquid (glycerol), we have observed stable formation of annular embossed patterns, the configuration of which, at a constant delay between pulses of $200\,\mu s$, is controlled solely by varying the laser pulse energy. High reproducibility of annular embossed patterns in glycerol makes it possible to use this method for modifying the silicon surface for applications. On the contrary, in water, the generation of axisymmetric annular embossed patterns is observed in a limited range of $[0.75–0.85]F_a$. Even at fluences near $0.9F_a$, several chaotically located annular embossed patterns are formed, which is associated with the collapse of the primary cavitation bubble in water into several secondary (persistent) gas bubbles.

TEM studies show that the superficial layer of 50–90 nm in thickness of the fabricated annular embossed patterns (including hillock and doughnut-shaped rims) is mainly amorphous with small inclusions of nanocrystallites, indicating melting and rapid crystallization of the layer. The observed asymmetry of the inner and outer rims surrounding the annular microdimple (groove) reflects the direction of melt motion from hotter areas corresponding to the maxima of the diffraction ring pattern. In addition, overhanging of the solidified melt of the inner doughnut-shaped rim above the surface with the formation of above-surface cavities (shelters) at certain fluences was found out, which was not previously observed using AFM and SEM.

We have performed 3D full-wave electromagnetic modeling of laser light diffraction by a bubble in glycerol near the silicon surface to determine the electric field within silicon. It is shown, that the maximal intensity field is 1.7 times larger than for laser light propagating through bubble-free glycerol. As a result, the diffracted light intensity in silicon exceeds the melting and surface modification thresholds at diffraction maxima for all fluences considered. Moreover, we have determined possible radii and positions of bubbles relative to the silicon surface for various pulse fluences. It is found that the bubble radii increase monotonically with the increase of pulse fluence reaching $1.8\,\mu m$ in the case of a full-spherical bubble and $2.4\,\mu m$ in the case of a hemispherical bubble for the fluence of $1.28F_a$.

As a result of amplification the light intensity concentrated in one narrow diffraction ring, a specific annular groove surrounded by two rims is formed on the silicon surface. We have demonstrated in the large-scale MD simulations that the fast heating in the diffraction peak generates a large pressure gradient in the plane of heated layer, which pushes the molten silicon out of the groove. After rapid cooling, the ejected (redistributed) melt solidifies in the form of two rims on the groove edges.

It is worth noting high reproducibility of the formation of annular embossed patterns, and hence the process of bubble (the laser intensity modulator) formation. Notwithstanding the combination of complex mechanisms and effects, shot-to-shot reproducibility of the energy of laser pulses plays a crucial role. At the same time, the specific type of annular embossed patterns may be easily controlled through variation of laser energy, wavelength and a number of pulses. This allows to fabricate regular arrays on a substrate, that could be further potentially used in various applications.

CRediT authorship contribution statement

S.A. Romashevskiy: Conceptualization, Investigation, Writing – original draft, Visualization. **A.I. Ignatov:** Software, Methodology, Writing – original draft. **V.V. Zhakhovsky:** Software, Methodology, Writing – original draft. **E.M. Eganova:** Investigation. **E.A. Pershina:** Investigation. **N.A. Inogamov:** Formal analysis, Methodology. **S.I. Ashitkov:** Conceptualization, Writing – original draft, Supervision.

Declaration of competing interest

The authors declare that they have no known competing financial interests or personal relationships that could have appeared to influence the work reported in this paper.

Data availability

Data will be made available on request.

Acknowledgments

This work was supported by Russian Science Foundation (grant 19-19-00697-P). The experiments on laser–matter interaction were performed in the “Femtosecond Laser Center” of the Joint Institute for High Temperatures of the Russian Academy of Sciences.

References

[1] K.C. Phillips, H.H. Gandhi, E. Mazur, S.K. Sundaram, Ultrafast laser processing of materials: a review, Adv. Opt. Photonics 7 (4) (2015) 684, http://dx.doi.org/10.1364/AOP.7.000684.

[2] M. Malinauskas, A. Žukauskas, S. Hasegawa, Y. Hayasaki, V. Mizeikis, R. Buividas, S. Juodkazis, Ultrafast laser processing of materials: from science to industry, Light Sci. Appl. 5 (8) (2016) e16133, http://dx.doi.org/10.1038/lsa.2016.133.

[3] K. Sugioka, Progress in ultrafast laser processing and future prospects, Nanophotonics 6 (2) (2017) 393–413, http://dx.doi.org/10.1515/nanoph-2016-0004.

[4] S.M. Yalisove, K. Sugioka, C.P. Grigoropoulos, Advances and opportunities of ultrafast laser synthesis and processing, MRS Bull. 41 (12) (2016) 955–959, http://dx.doi.org/10.1557/mrs.2016.273.

[5] J.B. Baxter, C. Richter, C.A. Schmuttenmaer, Ultrafast carrier dynamics in nanostructures for solar fuels, Ann. Rev. Phys. Chem. 65 (1) (2014) 423–447, http://dx.doi.org/10.1146/annurev-physchem-040513-103742.

[6] S. Chang, X. Guo, X. Ni, Optical metasurfaces: Progress and applications, Annu. Rev. Mater. Res. 48 (1) (2018) 279–302, http://dx.doi.org/10.1146/annurev-matsci-070616-124220.

[7] P.L. Stiles, J.A. Dieringer, N.C. Shah, R.P. Van Duyne, Surface-enhanced Raman spectroscopy, Annu. Rev. Anal. Chem. 1 (1) (2008) 601–626, http://dx.doi.org/10.1146/annurev.anchem.1.031207.112814.

[8] S. Syubaev, E. Mitsai, S. Starikov, A. Kuchmizhak, Laser-printed hemispherical silicon Mie resonators, Opt. Lett. 46 (10) (2021) 2304, http://dx.doi.org/10.1364/OL.425809.

[9] S.V. Makarov, A.S. Zalogina, M. Tajik, D.A. Zuev, M.V. Rybin, A.A. Kuchmizhak, S. Juodkazis, Y. Kivshar, Light-induced tuning and reconfiguration of nanophotonic structures, Laser Photonics Rev. 11 (5) (2017) 1700108, http://dx.doi.org/10.1002/lpor.201700108.

[10] R. Streubel, S. Barcikowski, B. Gökce, Continuous multigram nanoparticle synthesis by high-power, high-repetition-rate ultrafast laser ablation in liquids, Opt. Lett. 41 (7) (2016) 1486, http://dx.doi.org/10.1364/ol.41.001486.

[11] D. Pavlov, S. Gurbatov, S.I. Kudryashov, P.A. Danilov, A.P. Porfirev, S.N. Khonina, O.B. Vitrik, S.A. Kulinich, M. Lapine, A.A. Kuchmizhak, 10-Million-elements-per-second printing of infrared-resonant plasmonic arrays by multiplexed laser pulses, Opt. Lett. 44 (2) (2019) 283, http://dx.doi.org/10.1364/OL.44.000283.

[12] L. Jiang, A.-D. Wang, B. Li, T.-H. Cui, Y.-F. Lu, Electrons dynamics control by shaping femtosecond laser pulses in micro/nanofabrication: modeling, method, measurement and application, Light Sci. Appl. 7 (2) (2018) 17134, http://dx.doi.org/10.1038/lsa.2017.134.

[13] M.G. Rahimian, F. Bouchard, H. Al-Khazraji, E. Karimi, P.B. Corkum, V.R. Bhardwaj, Polarization dependent nanostructuring of silicon with femtosecond vortex pulse, APL Photonics 2 (8) (2017) http://dx.doi.org/10.1063/1.4999219.

[14] F. Takahashi, K. Miyamoto, H. Hidai, K. Yamane, R. Morita, T. Omatsu, Picosecond optical vortex pulse illumination forms a monocrystalline silicon needle, Sci. Rep. 6 (1) (2016) 21738, http://dx.doi.org/10.1038/srep21738.

[15] M. Zukerstein, J. Hrabovsky, J. Sladek, I. Mirza, Y. Levy, N. Bulgakova, Formation of tubular structures and microneedles on silicon surface by doughnut-shaped ultrashort laser pulses, Appl. Surface Sci. 592 (March) (2022) 153228, http://dx.doi.org/10.1016/j.apsusc.2022.153228.

[16] M.G. Rahimian, A. Jain, H. Larocque, P.B. Corkum, E. Karimi, V.R. Bhardwaj, Spatially controlled nano-structuring of silicon with femtosecond vortex pulses, Sci. Rep. 10 (1) (2020) 0–6, http://dx.doi.org/10.1038/s41598-020-69390-4.

[17] S. Syubaev, E. Mitsai, A. Porfirev, S. Khonina, S. Kudryashov, T. Katkus, S. Juodkazis, E.L. Gurevich, A. Kuchmizhak, Silicon microprotrusions with tailored chirality enabled by direct femtosecond laser ablation, Opt. Lett. 45 (11) (2020) 3050, http://dx.doi.org/10.1364/ol.393979.

[18] S. Syubaev, A. Zhizhchenko, O. Vitrik, A. Porfirev, S. Fomchenkov, S. Khonina, S. Kudryashov, A. Kuchmizhak, Chirality of laser-printed plasmonic nanoneedles tunable by tailoring spiral-shape pulses, Appl. Surface Sci. 470 (November 2018) (2019) 526–534, http://dx.doi.org/10.1016/j.apsusc.2018.11.128.

[19] D. Pavlov, A. Porfirev, S. Khonina, L. Pan, S.I. Kudryashov, A.A. Kuchmizhak, Coaxial hole array fabricated by ultrafast femtosecond-laser processing with spatially multiplexed vortex beams for surface enhanced infrared absorption, Appl. Surface Sci. 541 (September 2020) (2021) 148602, http://dx.doi.org/10.1016/j.apsusc.2020.148602.

[20] D. Pavlov, S. Syubaev, A. Cherepakhin, A. Sergeev, O. Vitrik, A. Zakharenko, P. Danilov, I. Saraeva, S. Kudryashov, A. Porfirev, A. Kuchmizhak, Ultrafast laser printing of self-organized bimetallic nanotextures for multi-wavelength biosensing, Sci. Rep. 8 (1) (2018) 1–10, http://dx.doi.org/10.1038/s41598-018-34784-y.

[21] D. Zhang, B. Gökce, S. Barcikowski, Laser synthesis and processing of colloids: Fundamentals and applications, Chem. Rev. 117 (5) (2017) 3990–4103, http://dx.doi.org/10.1021/acs.chemrev.6b00468.

[22] S.A. Romashevskiy, S.I. Ashitkov, M.B. Agranat, Surface microcavities at nanoscale depths produced by ultrafast laser pulses, Appl. Phys. Lett. 109 (26) (2016) 261601, http://dx.doi.org/10.1063/1.4973195.

[23] S. Romashevskiy, S. Ashitkov, A. Ovchinnikov, P. Kondratenko, M. Agranat, Formation of periodic mesoscale structures arranged in a circular symmetry at the silicon surface exposed to radiation of a single femtosecond laser pulses, Appl. Surf. Sci. 374 (2016) 12–18, http://dx.doi.org/10.1016/j.apsusc.2015.07.112.

[24] S.A. Romashevskiy, S.I. Ashitkov, M.B. Agranat, Circular ripple patterns on silicon induced by bubble-diffracted femtosecond laser pulses in liquid, Opt. Lett. 45 (4) (2020) 1005, http://dx.doi.org/10.1364/OL.385672.

[25] C.B. Schaffer, N. Nishimura, E.N. Glezer, A.M.-T. Kim, E. Mazur, Dynamics of femtosecond laser-induced breakdown in water from femtoseconds to microseconds, Opt. Express 10 (3) (2002) 196, http://dx.doi.org/10.1364/OE.10.000196.

[26] S. Reich, A. Letzel, A. Menzel, N. Kretzschmar, B. Gökce, S. Barcikowski, A. Plech, Early appearance of crystalline nanoparticles in pulsed laser ablation in liquids dynamics, Nanoscale 11 (14) (2019) 6962–6969, http://dx.doi.org/10.1039/c9nr01203f.

[27] C.-Y. Shih, R. Streubel, J. Heberle, A. Letzel, M.V. Shugaev, C. Wu, M. Schmidt, B. Gökce, S. Barcikowski, L.V. Zhigilei, Two mechanisms of nanoparticle generation in picosecond laser ablation in liquids: the origin of the bimodal size distribution, Nanoscale 10 (15) (2018) 6900–6910, http://dx.doi.org/10.1039/C7NR08614H.

[28] J. Tomko, S. O'Malley, C. Trout, J. Naddeo, R. Jimenez, J.C. Griepenburg, W. Soliman, D. Bubb, Cavitation bubble dynamics and nanoparticle size distributions in laser ablation in liquids, Colloids Surf. A 522 (2017) 368–372, http://dx.doi.org/10.1016/j.colsurfa.2017.03.030.

[29] M.K. Bhuyan, A. Soleilhac, M. Somayaji, T.E. Itina, R. Antoine, R. Stoian, High fidelity visualization of multiscale dynamics of laser-induced bubbles in liquids containing gold nanoparticles, Sci. Rep. 8 (1) (2018) 9665, http://dx.doi.org/10.1038/s41598-018-27663-z.

[30] C.-Y. Shih, M.V. Shugaev, C. Wu, L.V. Zhigilei, The effect of pulse duration on nanoparticle generation in pulsed laser ablation in liquids: insights from large-scale atomistic simulations, Phys. Chem. Chem. Phys. 22 (13) (2020) 7077–7099, http://dx.doi.org/10.1039/D0CP00608D.

[31] Y. Petrov, V. Khokhlov, V. Zhakhovsky, N. Inogamov, Hydrodynamic phenomena induced by laser ablation of metal into liquid, Appl. Surface Sci. 492 (October 2018) (2019) 285–297, http://dx.doi.org/10.1016/j.apsusc.2019.05.325.

[32] N.A. Inogamov, S.A. Romashevskiy, A.I. Ignatov, V.V. Zhakhovsky, V.A. Khokhlov, E.M. Eganova, E.A. Pershina, S.I. Ashitkov, Diffraction on a microbubble and the morphology of the silicon surface irradiated through glycerol by a pair of femtosecond laser pulses, JETP Lett. 113 (2) (2021) 75–81, http://dx.doi.org/10.1134/S0021364021020065.

[33] E.N. Glezer, C.B. Schaffer, N. Nishimura, E. Mazur, Minimally disruptive laser-induced breakdown in water, Opt. Lett. 22 (23) (1997) 1817–1819, http://dx.doi.org/10.1364/OL.22.001817.

[34] H. Yonekubo, K. Katayama, T. Sawada, Formation of a ripple pattern at a water/silicon interface using an oscillating bubble, Appl. Phys. A 81 (4) (2005) 843–846, http://dx.doi.org/10.1007/s00339-005-3269-2.

[35] K. Katayama, H. Yonekubo, T. Sawada, Laser processing at solid-liquid interfaces using femtosecond pulse laser sources, in: Fourth International Symposium on Laser Precision Microfabrication. Vol. 5063, (May) 2003, p. 367, http://dx.doi.org/10.1063/1.1582372.

[36] K. Katayama, H. Yonekubo, T. Sawada, Formation of ring patterns surrounded by ripples by single-shot laser irradiation with ultrashort pulse width at the solid/liquid interface, Appl. Phys. Lett. 82 (24) (2003) 4244–4246, http://dx.doi.org/10.1063/1.1582372.

[37] M.Y. Shen, C.H. Crouch, J.E. Carey, E. Mazur, Femtosecond laser-induced formation of submicrometer spikes on silicon in water, Appl. Phys. Lett. 85 (23) (2004) 5694–5696, http://dx.doi.org/10.1063/1.1828575.

[38] G. Daminelli, J. Krüger, W. Kautek, Femtosecond laser interaction with silicon under water confinement, Thin Solid Films 467 (1–2) (2004) 334–341, http://dx.doi.org/10.1016/j.tsf.2004.04.043.

[39] Z. Kan, Q. Zhu, H. Ren, M. Shen, Femtosecond laser-induced thermal transport in silicon with liquid cooling bath, Materials 12 (13) (2019) 10–13, http://dx.doi.org/10.3390/ma12132043.

[40] K. Affolter, W. Lüthy, M. Wittmer, Interference effects on the surface of Nd:YAG-laser-reacted Pd-silicide, Appl. Phys. Lett. 36 (7) (1980) 559–561, http://dx.doi.org/10.1063/1.91545.

[41] M. Senegačnik, P. Gregorčič, Diffraction-driven laser surface nanostructuring: Towards patterning with curved periodic surface structures, Appl. Surface Sci. (2022) 155486, http://dx.doi.org/10.1016/j.apsusc.2022.155486.

[42] S.A. Romashevskiy, Singularities of silicon surface nanostructuring due to ultrafast heating in water by a femtosecond laser pulse, Techn. Phys. Lett. 44 (7) (2018) 630–633, http://dx.doi.org/10.1134/S1063785018070271.

[43] S.A. Romashevskiy, Modifying silicon surface with single femtosecond laser pulses at near-threshold fluences in different media, in: Frontiers in Optics / Laser Science, Optica Publishing Group, 2020, http://dx.doi.org/10.1364/FIO.2020.JW6B.14, JW6B.14.

[44] N. Smirnov, S. Kudryashov, A. Rudenko, D. Zayarny, A. Ionin, Pulsewidth and ambient medium effects during ultrashort-pulse laser ablation of silicon in air and water, Appl. Surface Sci. 562 (2021) 150243, http://dx.doi.org/10.1016/j.apsusc.2021.150243.

[45] N.A. Smirnov, S.I. Kudryashov, P.A. Danilov, A.A. Rudenko, A.A. Ionin, A.A. Nastulyavichus, Silicon ablation by single ultrashort laser pulses of variable width in air and water, JETP Lett. 108 (6) (2018) 368–373, http://dx.doi.org/10.1134/S002136401818011X.

[46] S. van der Linden, R. Hagmeijer, G. Römer, Picosecond pulsed underwater laser ablation of silicon and stainless steel: Comparing crater analysis methods and analysing dependence of crater characteristics on water layer thickness, Appl. Surface Sci. 540 (November 2020) (2021) 148005, http://dx.doi.org/10.1016/j.apsusc.2020.148005.

[47] H. Liu, F. Chen, X. Wang, Q. Yang, H. Bian, J. Si, X. Hou, Influence of liquid environments on femtosecond laser ablation of silicon, Thin Solid Films 518 (18) (2010) 5188–5194, http://dx.doi.org/10.1016/j.tsf.2010.04.043.

[48] J. Ren, M. Kelly, L. Hesselink, Laser ablation of silicon in water with nanosecond and femtosecond pulses, Opt. Lett. 30 (13) (2005) 1740, http://dx.doi.org/10.1364/OL.30.001740.

[49] J.M. Liu, Simple technique for measurements of pulsed Gaussian-beam spot sizes, Opt. Lett. 7 (5) (1982) 196, http://dx.doi.org/10.1364/ol.7.000196.

[50] J. Bonse, K.W. Brzezinka, A.J. Meixner, Modifying single-crystalline silicon by femtosecond laser pulses: An analysis by micro Raman spectroscopy, scanning laser microscopy and atomic force microscopy, Appl. Surface Sci. 221 (1–4) (2004) 215–230, http://dx.doi.org/10.1016/S0169-4332(03)00881-X.

[51] N. Inogamov, V. Zhakhovsky, S. Ashitkov, Y. Emirov, A. Faenov, Y. Petrov, V. Khokhlov, M. Ishino, B. Demaske, M. Tanaka, N. Hasegawa, M. Nishikino, S. Tamotsu, T. Pikuz, I. Skobelev, T. Ohba, T. Kaihori, Y. Ochi, T. Imazono, Y. Fukuda, M. Kando, Y. Kato, T. Kawachi, S. Anisimov, M. Agranat, I. Oleynik, V. Fortov, Surface nanodeformations caused by ultrashort laser pulse, Eng. Fail. Anal. 47 (2015) 328–337, http://dx.doi.org/10.1016/j.engfailanal.2013.12.009.

[52] D.S. Ivanov, V.P. Lipp, A. Blumenstein, F. Kleinwort, V.P. Veiko, E. Yakovlev, V. Roddatis, M.E. Garcia, B. Rethfeld, J. Ihlemann, P. Simon, Experimental and theoretical investigation of periodic nanostructuring of Au with ultrashort UV laser pulses near the damage threshold, Phys. Rev. Appl. 4 (2015) 064006, http://dx.doi.org/10.1103/PhysRevApplied.4.064006.

[53] M. Garcia-Lechuga, D. Puerto, Y. Fuentes-Edfuf, J. Solis, J. Siegel, Ultrafast moving-spot microscopy: Birth and growth of laser-induced periodic surface structures, ACS Photonics 3 (10) (2016) 1961–1967, http://dx.doi.org/10.1021/acsphotonics.6b00514.

[54] M. Garcia-Lechuga, N. Casquero, A. Wang, D. Grojo, J. Siegel, Deep silicon amorphization induced by femtosecond laser pulses up to the mid-infrared, Adv. Opt. Mater. 9 (17) (2021) 2100400, http://dx.doi.org/10.1002/adom.202100400.
[55] J. Bonse, All-optical characterization of single femtosecond laser-pulse-induced amorphization in silicon, Appl. Phys. A 84 (1–2) (2006) 63–66, http://dx.doi.org/10.1007/s00339-006-3583-3.
[56] M.-R. Kalus, N. Bärsch, R. Streubel, E. Gökce, S. Barcikowski, B. Gökce, How persistent microbubbles shield nanoparticle productivity in laser synthesis of colloids — quantification of their volume, dwell dynamics, and gas composition, Phys. Chem. Chem. Phys. 19 (2017) 7112–7123, http://dx.doi.org/10.1039/C6CP07011F.
[57] D.C.K. Rao, V.S. Mooss, Y.N. Mishra, D. Hanstorp, Controlling bubble generation by femtosecond laser-induced filamentation, Sci. Rep. 12 (1) (2022) 15742, http://dx.doi.org/10.1038/s41598-022-20066-1.
[58] J.S. Hoppius, S. Maragkaki, A. Kanitz, P. Gregorčič, E.L. Gurevich, Optimization of femtosecond laser processing in liquids, Appl. Surface Sci. 467–468 (2019) 255–260, http://dx.doi.org/10.1016/j.apsusc.2018.10.121.
[59] C. Schinke, P. Christian Peest, J. Schmidt, R. Brendel, K. Bothe, M.R. Vogt, I. Kröger, S. Winter, A. Schirmacher, S. Lim, H.T. Nguyen, D. MacDonald, Uncertainty analysis for the coefficient of band-to-band absorption of crystalline silicon, AIP Adv. 5 (6) (2015) 067168, http://dx.doi.org/10.1063/1.4923379.
[60] J. Long, M. Eliceiri, Z. Vangelatos, Y. Rho, L. Wang, Z. Su, X. Xie, Y. Zhang, C.P. Grigoropoulos, Early dynamics of cavitation bubbles generated during ns laser ablation of submerged targets, Opt. Express 28 (10) (2020) 14300, http://dx.doi.org/10.1364/OE.391584.
[61] R. Tanabe, T.T. Nguyen, T. Sugiura, Y. Ito, Bubble dynamics in metal nanoparticle formation by laser ablation in liquid studied through high-speed laser stroboscopic videography, Appl. Surface Sci. 351 (2015) 327–331, http://dx.doi.org/10.1016/j.apsusc.2015.05.030.
[62] J. Lam, J. Lombard, C. Dujardin, G. Ledoux, S. Merabia, D. Amans, Dynamical study of bubble expansion following laser ablation in liquids, Appl. Phys. Lett. 108 (7) (2016) 074104, http://dx.doi.org/10.1063/1.4942389.
[63] M. Dell'Aglio, R. Gaudiuso, O. De Pascale, A. De Giacomo, Mechanisms and processes of pulsed laser ablation in liquids during nanoparticle production, Appl. Surface Sci. 348 (2015) 4–9, http://dx.doi.org/10.1016/j.apsusc.2015.01.082.
[64] T. Hupfeld, G. Laurens, S. Merabia, S. Barcikowski, B. Gökce, D. Amans, Dynamics of laser-induced cavitation bubbles at a solid–liquid interface in high viscosity and high capillary number regimes, J. Appl. Phys. 127 (4) (2020) 044306, http://dx.doi.org/10.1063/1.5116111.
[65] S. Kohsakowski, B. Gökce, R. Tanabe, P. Wagener, A. Plech, Y. Ito, S. Barcikowski, Target geometry and rigidity determines laser-induced cavitation bubble transport and nanoparticle productivity – a high-speed videography study, Phys. Chem. Chem. Phys. 18 (24) (2016) 16585–16593, http://dx.doi.org/10.1039/C6CP01232A.
[66] S. Reich, P. Schönfeld, P. Wagener, A. Letzel, S. Ibrahimkutty, B. Gökce, S. Barcikowski, A. Menzel, T. dos Santos Rolo, A. Plech, Pulsed laser ablation in liquids: Impact of the bubble dynamics on particle formation, J. Colloid Interface Sci. 489 (2017) 106–113, http://dx.doi.org/10.1016/j.jcis.2016.08.030.
[67] V.V. Zhakhovsky, Tabulated EAM potential for water can be downloaded from https://www.researchgate.net/project/Development-of-interatomic-EAM-potentials.
[68] V.V. Zhakhovskii, N.A. Inogamov, Y.V. Petrov, S.I. Ashitkov, K. Nishihara, Molecular dynamics simulation of femtosecond ablation and spallation with different interatomic potentials, Appl. Surf. Sci. 255 (24) (2009) 9592–9596, http://dx.doi.org/10.1016/j.apsusc.2009.04.082.
[69] S. Murzov, S. Ashitkov, E. Struleva, P. Komarov, V. Zhakhovsky, V. Khokhlov, N. Inogamov, Elastoplastic and polymorphic transformations of iron at ultra-high strain rates in laser-driven shock waves, J. Appl. Phys. 130 (24) (2021) 245902, http://dx.doi.org/10.1063/5.0076869.